Digital Communications over the Audio Channel

Diploma Thesis

Signal Processing and Speech Communication Laboratory
Graz University of Technology

by
Karl Maier

Supervisors
Assoc.Prof. DI Dr. Klaus Witrisal
Dipl.-Ing. Andreas Pedroß

Head of the Institute: Univ.-Prof. DI Dr.techn. Gernot Kubin

A - 8010 Graz, Inffeldgasse 16c
Telefon: (+43 316) 873 - 4430
http://www.spsc.tugraz.at
http://www.tugraz.at

Graz / December - 2011

Statutory Declaration

I declare that I have authored this thesis independently, that I have not used other than the declared sources/resources, and that I have explicitly marked all material which has been quoted either literally or by content from the used sources.

date

(signature)

Abstract

Ultra-wideband (UWB) systems are a promising technology for short-range communications. The huge bandwidth of such systems gives the opportunity to achieve high data rates without the need for modulation schemes that would require a very high signal-to-noise ratio (SNR). This diploma thesis describes the design and implementation of a non-coherent, digital communication system for high data rates over a time-variant indoor audio channel. This kind of communication channel shares many characteristics with RF UWB channels, well studied for wireless RF communications. Besides the big delay spread, the Doppler effect does represent a big influence and difficulty due to the low propagation speed of the acoustic signals. The modulation scheme was chosen to be a multicarrier pulse-position modulation (multicarrier PPM) scheme. The receiver was designed and implemented as a frequency-separating energy-detector and it was possible to achieve a data rate of 285bit/s. BER simulations have shown a significant but constant performance gap w.r.t. an optimal coherent receiver over an AWGN channel due to the severe channel-induced signal distortions and the non-coherent receiver. Because of the lack of appropriate channel models, the present audio channel was measured with a channel sounding method and a time-variant channel model was implemented. This model was used later for the simulation of the transmission system. Furthermore, this thesis discusses properties of the channel by showing some of the measured impulse responses, average power delay profiles and Doppler power spectra. It becomes evident that high-frequency components of the impulse responses decay clearly faster than low-frequency ones. Another evaluated property of the channel is the fastly increasing fading rate at higher frequency ranges due to the Doppler spread.

Kurzfassung

Ultra-Breitbandsysteme (engl. ultra-wideband, UWB) stellen eine vielversprechende Technologie auf dem Gebiet der Nahbereichsfunkkommunikation dar. Die große Bandbreite von solchen Systemen bietet die Möglichkeit, hohe Datenraten zu erreichen, ohne dass dazu Modulationsverfahren benötigt werden, die einen sehr hohen Signal-Rausch-Abstand (SNR) benötigen. Diese Diplomarbeit beschäftigt sich mit der Implementierung eines nicht-kohärenten, digitalen Datenübertragungssystems für hohe Datenraten über einen zeitvarianten Innenraum-Audiokanal. Dieser Kanal ähnelt in vielen Belangen den aus Drahtloskommunikationssystemen bekannten UWB Kanälen. Dabei stellt neben dem großen Delay Spread, aufgrund der geringen Wellenausbreitungsgeschwindigkeit der akustischen Signale, der Doppler Effekt eine große Einflußgröße und Schwierigkeit dar. Als Modulationsverfahren wurde eine Mehrkanal-Pulspositionsmodulation gewählt. Der Empfänger wurde als Energie-Detektor konzipiert und implementiert. Es wurde eine Datenrate von bis zu 285 Bit/s erreicht. Bitfehlersimulationen haben einen signifikanten, aber konstanten Performanceunterschied im Vergleich zu einem kohärenten Empfänger im AWGN-Kanal gezeigt, der auf die starken kanalinduzierten Signalverzerrungen und den nicht-kohärenten Empfänger zurückzuführen ist. Aufgrund fehlender Kanalmodelle wurde der vorliegende Übertragungskanal mit einer Channel Sounding Methode vermessen und ein zeitvariantes Kanalmodell implementiert, welches für die spätere Simulation des Übertragungssystems diente. Weiters werden in der Arbeit Eigenschaften des Kanals in Form von gemessenen Impulsantworten, Average Power Delay Profiles und Doppler Power Spectra aufgezeigt. Dabei wird ersichtlich, dass hochfrequente Anteile der Impulsantworten deutlich schneller abfallen als niederfrequente. Eine weitere Eigenschaft des Kanals, eine stark ansteigende Fadingrate in höheren Frequenzbereichen aufgrund des Doppler Spreads, wird ebenfalls gezeigt.

Acknowledgement

First of all I want to thank my family for their moral and financial support. Without them, this diploma thesis and more general, my studies at the TU Graz wouldn't have been possible. Furthermore I want to thank my supervisors, Klaus Witrisal and Andreas Pedroß, for their support and their patience regarding my never-ending questions and doubts.

Contents

1 Introduction **6**
- 1.1 Motivation . . . 6
- 1.2 Overview . . . 6
- 1.3 Outline . . . 7

2 Acoustic digital communication system **8**
- 2.1 System model . . . 8
- 2.2 Time-varying acoustic channel model . . . 10
  - 2.2.1 LOS and NLOS . . . 13
  - 2.2.2 APDP, Delay spread and K-factor . . . 13
  - 2.2.3 Doppler spread . . . 14

3 Channel measurements **17**
- 3.1 Identifiability of the channel . . . 17
  - 3.1.1 Maximum length sequences . . . 18
- 3.2 Scenario setup . . . 22
- 3.3 Channel parameter evaluation . . . 25
  - 3.3.1 LOS and NLOS . . . 25
  - 3.3.2 APDP, delay spread & K-factor . . . 27
  - 3.3.3 Doppler spread . . . 28
- 3.4 Channel Transfer Function . . . 34
- 3.5 Subcarrier Impulse Responses . . . 35
- 3.6 Time-variability of the channel . . . 38
- 3.7 Simulation framework . . . 39
  - 3.7.1 Interpolation between the measured CIR . . . 40
  - 3.7.2 Memory requirements . . . 40

4 System design **41**
- 4.1 Signaling . . . 43
- 4.2 Transmitter . . . 48
  - 4.2.1 Frequency spacing of the carriers . . . 49
  - 4.2.2 Symbol rate per carrier . . . 51
- 4.3 Receiver . . . 51
  - 4.3.1 Block size and frequency resolution . . . 53
  - 4.3.2 Integration window . . . 54

5 Receiver performance evaluation **55**

6 Conclusion **60**

A Appendix **62**
- A.1 Illustrations of the physical channel setup and the used software 62
- A.2 Datasheets . . . 65

List of symbols

Uppercase:

B	Bandwidth
B_c	Channel coherence bandwidth
B_f	Fractional bandwidth
B_G	Guard band
B_p	Pulse bandwidth
B_{rec}	Integration bandwidth of the receiver
$B_{rec,D}$	Integration bandwidth of the receiver (with Doppler spread)
$\underline{H}$	Matrix representation of the time-variant channel impulse responses
$H(t,\omega)$	Channel transfer function
$H_{av}(\omega)$	Average channel transfer function
K_{LOS}	Ricean K-factor
L	Length of a MLS
M_{mat}	Number of columns of the channel impulse response matrix
N	Number of symbol durations
N_{bl}	Block length in samples for FFT
N_c	Number of carriers
N_I	Integration intervall in samples
N_{mat}	Number of rows of the channel impulse response matrix
N_p	Number of power delay profiles
N_{ss}	Number of measured snapshots
$P(\tau)$	Average power delay profile
P_0	Normalized power
R_b	Bit rate of the transmission system
S_{double}	Required memory for data type 'double'
S_{mem}	Required memory for the channel impulse response matrix
T	Sampling time

T_{bl}	Block length in seconds
T_c	Channel coherence time
T_I	Integration intervall in seconds
T_i	Impulse response duration
T_{MLS}	Period of a MLS
T_p	Time period between two consecutive fading dips
T_{rep}	Maximum repetition time interval for channel sounding
T_s	Symbol duration

Lowercase:

c	Propagation speed of the electromagnetic wave
c_a	Propagation speed of the acoustic wave
f	Frequency
f_k	Frequency of a sinusoidal carrier
f_H	Maximum frequency of a signal
f_L	Minimum frequency of a signal
f_{rep}	Minimum temporal sampling rate for channel sounding
f_{res}	Frequency resolution at the receiver
f_s	Sampling frequency
$g(t)$	Baseband pulseshape
$\underline{h}^T$	Channel impulse response (vector notation)
$\underline{h_n}^T$	Non-static channel impulse response (vector notation)
$h(t)$	Channel impulse response (time-continuous)
$h[n]$	Channel impulse response (time discrete)
$h'[n]$	Periodic channel impulse response
$h_n[n]$	Non-static channel impulse response
k	Correction factor for corresponding frequency bands
m	Order of a MLS
r	Roll-off factor

r_c	Symbol rate per carrier
s_k	Bit value
$s(t)$	Periodic impulse train
t	Time
$\underline{u}$	Detected symbol vector
v	Movement speed of the receiver
v_{RF}	Movement speed of the receiver in the RF channel
W	Absolute bandwidth
W_0	Minimum Nyquist bandwidth
$x(t)$	Transmitted signal (time-continuous)
$x[n]$	Transmitted signal (time discrete)
$x'[n]$	Periodic input signal
$\underline{x}[n]$	Transmitted signal (vector notation)
$y(t)$	Received signal (time-continuous)
$y[n]$	Received signal (time discrete)
$\underline{y}[n]$	Received signal vector (time discrete)
$y'[n]$	Periodic output signal
$\underline{z}$	Decision variable vector
$\underline{z}_1$	Vector containing the energy of the first time slot on each carrier
$\underline{z}_2$	Vector containing the energy of the second time slot on each carrier

Uppercase Greek:

$\triangle f$	Frequency resolution of the MLS measurement
$\triangle f_c$	Frequency spacing between two adjacent carriers
$\triangle s$	Length of the receiver's trajectory
$\triangle t$	Movement time of the receiver between two adjacent snapshots in seconds
$\triangle n_s$	Movement time of the receiver between two adjacent snapshots in samples

$\triangle x$	Distance between two adjacent snapshots
$\triangle x_s$	Maximum distance between two adjacent snapshots
Π_k	Rectangular window in frequency domain
Ω'_{xx}	Renormalized periodic autocorrelation function
Ω'_{xy}	Renormalized periodic crosscorrelation function

Lowercase Greek:

$\underline{\beta}$	Complex channel factor (containing gain and phase shift)
γ	Angle between direction of movement and direction of wave propagation
$\delta(t)$	Dirac delta function
$\eta(t)$	Additive white Gaussian noise (time-continuous)
λ	Wavelength
ν	Doppler shift
ν_{rms}	RMS Doppler spread
$\bar{\nu}$	First moment of the Doppler power spectrum
$\overline{\nu^2}$	Second moment of the Doppler power spectrum
τ	Delay time
τ_{max}	Maximum excess delay
τ_{rms}	RMS delay spread
τ_s	Time slot duration
$\overline{\tau^2}$	Second moment of the Average power delay profile
$\overline{\tau_m}$	Mean excess delay
ϕ'_{xx}	Periodic autocorrelation function
ω	Angular frequency

1 Introduction

1.1 Motivation

UWB (ultra-wideband) systems are considered a promising technology for short-range communications as they can provide high data rates with possibly low power consumption. By virtue of the huge bandwidths inherent to UWB systems, great channel capacities can be achieved without the need to implement higher order modulation schemes which need very high signal-to-noise ratio (SNR) to operate properly. Possible applications could be wireless monitors, DVD players, communications between handheld devices like mobile phones, personal digital audio and video players but also radar systems and sensors for medical use. In order to be able to design and evaluate such a UWB system, it is important to have an accurate channel model. However, the available channel models are not yet sufficiently elaborate [1]. The possibility of measuring the channel and establishing a model based on the measurements requires high sampling rates due to the wide bandwidths and sophisticated hardware. Alternatively, as many wave propagation phenomena are similar in the radio and the acoustic audio channel [2], the audio channel can be used instead of the UWB radio channel.

1.2 Overview

In [3], a rather simple, low cost demonstration system for UWB applications is proposed, using the audio channel instead of the radio channel to evaluate possible UWB implementations at an early stage of development, using the analogy between electromagnetic and acoustic wave propagation. It was shown that, apart from different propagation speeds, there are no significant differences with respect to the channel parameters. This gives the oportunity to implement a cheap UWB demonstration system by using standard audio devices such as speakers and microphones. In this work, an indoor noncoherent communication system over the audio channel between a sender and a moving receiver was implemented. This presented a challenging task, knowing that the channel dictates the complexity and performance of the digital communication system and considering the high values of the expected delay spread and Doppler shift due to the low propagation speed of acoustic waves. As there were no channel models at hand, which would decribe the behaviour of the channel, it was necessary to identify (sound) the channel first. As a consequence, the objective of this diploma thesis was firstly to identify a time-variant acoustic indoor channel by channel sounding and to implement a time-variant channel model. In order to get some insight into the channel behavior and its impact on sent signals, important channel parameters, such as RMS delay spread and Doppler spread, were extracted. Secondly, based on the then known channel and its channel parameters, the next step was to choose an appropriate modulation scheme for the channel followed by the design and implementation of a basic digital communication system over the simulated channel. The final task was the evaluation

of the behaviour of the system using different transmission speeds and pulse shapes w.r.t. the bit-error-rate (BER).

1.3 Outline

In Chapter 2 the principles of an acoustic digital communication system and its equivalence with the radio channel are shown. A mathematical channel model is derived in order to model an acoustic channel. Also, important channel parameters and their impact on transmitted signals are explained. Chapter 3 explains the procedure of the channel measurements made for the given channel and the calculation of the channel parameters introduced in the previous section. The behavior of the channel and its impact on transmitted signals in time and frequency domain are examined in more detail. Also, an insight into the implementation of the mathematical channel model will be provided. Chapter 4 deals with choosing an adequate modulation scheme for the given channel and designing the transmitter and receiver structures. Furthermore, the implemented pulse shapes are presented. The obtained simulation results and the resulting BER curves for different transmission speeds and pulse shapes are shown in Chapter 5. In Chapter 6, a short conclusion and an outlook for future related work will be given.

2 Acoustic digital communication system

The objective of this work was to implement an acoustic digital communication system over an indoor channel in order to evaluate possible UWB implementations. To make sure that the acoustic channel can be considered to be a UWB system, the minimum bandwidth of a system has to fulfill either

$$B \geq 500MHz \tag{1}$$

or the fractional bandwidth B_f fulfills

$$B_f = 2\frac{f_H - f_L}{f_H + f_L} \geq 0.2 \tag{2}$$

where f_H denotes the maximum frequency of the transmitted signal and f_L the minimum frequency for the signal [4]. For the audio channel, the parameters are f_L=20Hz, f_H=20kHz, so that B_f=1.996, which fulfills the condition in (2), hence, it can be considered to be an ultra wideband channel. As already explained, in [3] it was shown that, with respect to the channel parameters such as RMS delay spread, K-factor, etc., there are no significant differences between the audio and the RF UWB radio channel apart from the impact of the different propagations speeds which can be corrected by a correction factor. A requirement for the comparability between the channels is the equivalence of wavelength. Using the relation between wavelength λ and frequency f given by the propagation speed of the electromagnetic wave c ($\lambda = \frac{c}{f}$ with $c = 3 \cdot 10^8$m/s), the corresponding wavelength for a maximum frequency of 10.6GHz is 2.83cm while for a minimum frequency of 3.1GHz (values for the RF UWB channel defined by the FCC) the wavelength is 9.67cm. The relation between the propagation speed of the acoustic and the radio wave (c_a and c, respectively) equals the correction factor k given as

$$k = \frac{c}{c_a} = \frac{3 \cdot 10^8 m/s}{343 m/s} = 8.746 \cdot 10^5 \tag{3}$$

with which the corresponding frequency ranges for audio and radio channel can be calculated. The transmission system in this work will use the whole frequency range of the audio channel from 20Hz up to 20kHz, the equivalent frequency range of the radio channel is shown in Table 1.

Frequency range	Audio channel	20Hz - 20kHz
	UWB channel	17.49MHz - 17.49GHz

Table 1: Table for the corresponding frequency range of audio and RF UWB channel, wavelength: 0.01715m - 17.15m

2.1 System model

This section will give an insight into the system model of a transmission system for an acoustic channel and the processing steps that are performed.

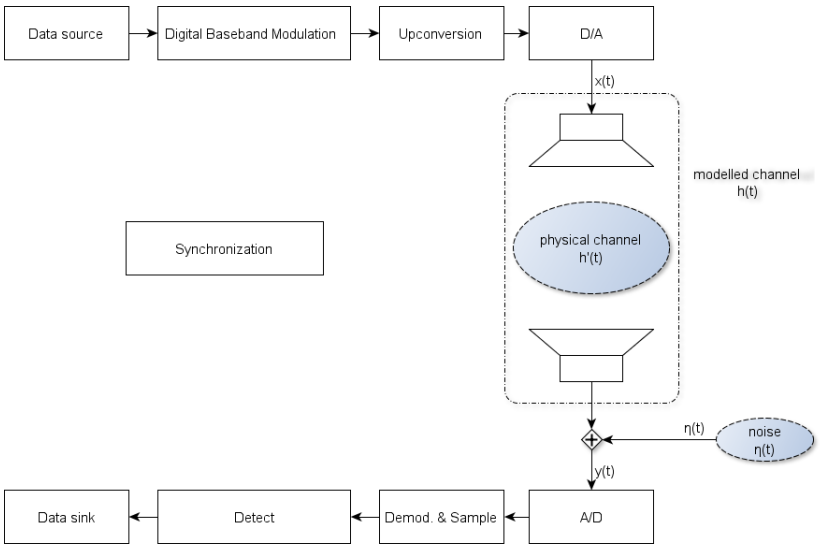

Figure 1: General communication system model

In Figure 1 the block diagram for the general system model of the acoustic communication system is shown. The upper half of the image shows the *sender* or *transmitter (TX)*, the lower half the *receiver (RX)*. The *Data source* provides the information to be transmitted in binary format (bits) and provides a bit stream as output signal. In the following block, *Digital Baseband Modulation,* the bits are converted to waveforms that are compatible with the requirements imposed by the transmission channel. This block also includes pulse shaping to ensure proper signal bandwidth when the signal is transmitted. The so obtained baseband waveforms at the output will be frequency translated to one or more carrier frequencies in order to shift them into the frequency band of the audio channel. This is done by the block denoted as upconversion. The following block contains the digital-to-analog conversion. The resulting waveforms are sent by a standard audio speaker, converting the electrical waveforms to acoustic ones. The receiver front-end consists of a microphone which converts the acoustic signals back to electrical ones. As these acoustic signals propagate over the channel, they are impacted by the channel characteristics $h'(t)$. The speaker, transmission channel and microphone form the so called communication channel which can be described as the channel impulse response $h(t)$ (also called CIR). The signal is also corrupted by additive, random noise which is denoted as $\eta(t)$ in the block diagram. The demodulator, shown in Figure 1 as *Demod. & Sample*-block, provides frequency down conversion for each sent waveform and creates a sampled version of the received signal which is used to obtain an estimate of the message symbol, the sent bit, by the following *Detect*-block. Note that, although synchronization is involved in the control of all signal processing in the shown blocks, there are no connecting lines drawn for simplicity.

2.2 Time-varying acoustic channel model

In this section, the mathematical description of a time-variant channel model will be derived, starting with the description of a linear time-invariant (LTI) discrete system and further describing the one for a time variant scenario.
The impulse response $h(t)$ of a linear, time-invariant channel with multipath propagation can be written as

$$h(t) = \sum_{i=0}^{\infty} \underline{\beta_i} \cdot \delta(t - \tau_i) \tag{4}$$

where the complex factors $\underline{\beta_i}$, denoting gain and phase shifts, and the delay times τ_i are time invariant, so the channel does not change in time domain. Figure 2 shows such a so called tapped delay line model graphically. Only the magnitude of the complex factors $\underline{\beta_i}$ is drawn in the illustration.

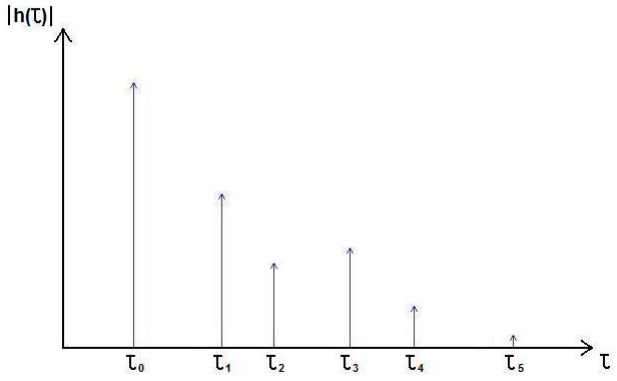

Figure 2: Magnitude of the impulse response h(τ) (schematic)

The received signal $y(t)$ can be described mathematically as the convolution of the transmitted signal $x(t)$ with the impulse response [5], given as

$$\begin{aligned} y(t) &= x(t) \star h(t) + \eta(t) && (5) \\ &= \int_{-\infty}^{\infty} x(\tau) h(t - \tau) d\tau + \eta(t) && (6) \\ &= \int_{-\infty}^{\infty} x(t - \tau) h(\tau) d\tau + \eta(t), && (7) \end{aligned}$$

where '$\star$' denotes the convolution operator and $\eta(t)$ the additive noise term. In digital communications, the signals are sampled and transformed into time discrete signals. Assuming that the Nyquist sampling theorem holds, that means,

that the highest frequency component of the continuous signal has a frequency below the half of the sample frequency, the convolution from (7) can be written in discrete time domain as [6]

$$\begin{aligned} y[n] &= x[n] \star h[n] + \eta[n] && (8) \\ &= \sum_{k=-\infty}^{\infty} h[k]x[n-k] + \eta[n] && (9) \\ &= \sum_{k=0}^{\infty} h[k]x[n-k] + \eta[n] && (10) \end{aligned}$$

where $h[n]$ is the time discrete impulse response and $\eta[n]$ the time discrete noise. Analogously, $x[n]$ and $y[n]$ are the sampled, time discrete input and output signals. For causal systems, there can be no output prior to the time instance n at which the input is applied, therefore the lower limit of the sum can be changed to zero in (10). For systems with an impulse response of finite length M_{mat}, (10) becomes

$$\begin{aligned} y[n] &= \sum_{k=0}^{N} h[k]x[n-k] + \eta[n] && (11) \\ &= \underline{h}^T \cdot \underline{x}[n] + \eta[n] && (12) \end{aligned}$$

with

$$\underline{h}^T \doteq \begin{bmatrix} h[0] & h[1] & h[2] & . & . & . & h[M_{mat}] \end{bmatrix}$$

and

$$\underline{x}[n] \doteq \begin{bmatrix} x[n-M_{mat}] \\ x[n-M_{mat}-1] \\ x[n-M_{mat}-2] \\ . \\ . \\ x[n-1] \\ x[n] \end{bmatrix},$$

where $\underline{x}[n]$ is the tap-input vector of the sent signal, $\underline{h}^T$ the vector containing the impulse response samples and $\eta[n]$ the samples of the additive noise. Note that the vector $\underline{h}^T$ consists of the samples $h[k]$ for $k = 0...M_{mat}$ and $\underline{x}[n]$ of $x[n-k]$ for $k = 0...M_{mat}$. A system as described in (11) can be relatively easily modeled using tapped delay line filters. In the case of this work, the channel is time-variant, so the impulse response $h[n]$ is not constant, which has to be taken into account for the transmission system and for the channel model as well. It will be shown later in this work that the time span in which the channel can be assumed to be approximately constant, the so-called channel coherence time, is much smaller than the chosen symbol period. For the transmission system this means that the channel can change significantly while only one symbol is

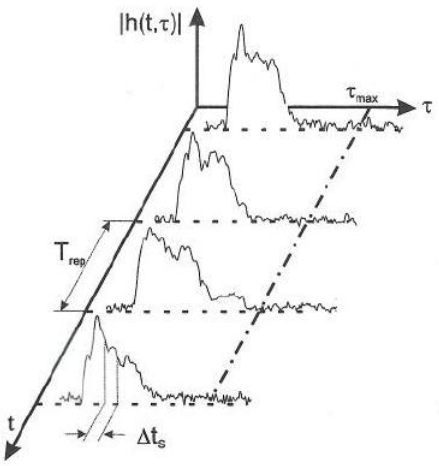

Figure 3: IR of a time-variant channel [7]

transmitted, which presents a big impairment that has to be taken in account when choosing an adequate modulation scheme. Figure 3 illustrates such a time-variant channel. In the following, the distinction between time-domain (denoted as t) and delay-domain (variable τ) has to be made. The illustration shows that, as the receiver moves through the room constantly, for any (absolute) time instance t the channel has a different impulse response and therefore the transmitted signal is affected differently. For the channel model this means that the impulse response with which the transmitted signal is convoluted is time-variant, so that the output signal $y[n]$ is given as

$$y[n] = \sum_{k=0}^{\infty} h_n[k]x[n-k] + \eta[n], \tag{13}$$

where the matematical description of a time-varying channel $h_n[k]$ denotes the non-static channel impulse response. For every single time instance n there exists an corresponding impulse response. Rewritten, we can also describe it as

$$y[n] = \underline{h_n}^T[n] \cdot \underline{x}[n] + \eta[n] \tag{14}$$

where the vector $\underline{h_n}^T[n]$ contains the non-static impulse response for the given time instance n. For the implementation of this channel model, the measured impulse responses $\underline{h_n}^T[n]$ are stored in the so called channel impulse response matrix $\underline{H}$. Every row in the $\underline{H}$-matrix corresponds to the impulse response at a given time instance n, whereas the columns represent the channel coefficients at a given discrete delay lag τ_i.

2.2.1 LOS and NLOS

It was already mentioned that the channel over which the digital communication system should be implemented is a time-variant acoustic indoor channel. In any environment, the acoustic waves propagate along different paths and undergo attenuation, reflection and diffraction on their way to the receiver and the resulting signal at the receiver will be a superposition of the multipath components (MPC), all arriving at different times, leading to interference effects. However, if there exists a direct path between transmitter and receiver, then a signal that propagates along this trajectory will arrive before all the other components and will also have a higher power level because it was not reflected on its way unlike all the other waves. This case is referred to as *line-of-sight (LOS)* scenario and the first arriving component is called *line-of-sight* or *dominant component*. In the contrary case, if no direct path between TX and RX exists, the scenario is called *non-line-of-sight (NLOS)*. All the MPCs are reflected on their way and therefore the arriving signal is, in general, weaker than the one in the LOS scenario. Also, the first arriving component is is in this case not necessarily the strongest one. The absence of a dominant component also leads to a stronger signal degradation because of the interference effects between the incident waves with similar power.

2.2.2 APDP, Delay spread and K-factor

Although channels may be very different, it is possible to evaluate their behavior by extracting specific channel parameters from their measured impulse responses (the description of the measurements can be found in chapter 3). The most important channel parameters and how to obtain them will be presented in this and the following subsection. First, the so called *Average Power Delay Profile* (APDP) is needed. From an ensemble of N_p impulse responses from various locations, the APDP $P(\tau)$ can be calculated by

$$P(\tau) = \overline{|h_i(\tau)|^2} = \frac{1}{N_p} \sum_{i=1}^{N_p} |h_i(\tau)|^2 \tag{15}$$

where $h_i(\tau)$ are the impulse responses for $i = 1...N_p$ [9]. It has to be noted that every PDP starts with the first detectable arriving signal, so the delay of the first detected signal has to be set to zero. The channel parameters will be exctracted from this APDP. The *normalized power* P_0 is obtained. It is the sum of power of all M incident waves. To calculate P_0, the maximum value of the incident wave will be normalized to the value 1 in order to eliminate the influence of the free-space loss, therefore it is defined as

$$P_0 = \sum_{i=1}^{M} \beta_i{}^2. \tag{16}$$

In order to find out how much energy is located in the strongest component (in the LOS case this is the direct path) the so called *Ricean K-factor* is calculated.

K_{LOS} gives the relationship between the power of the LOS component and the sum of the power of the MPCs and is given as

$$K_{LOS} = \frac{{\beta_i, max}^2}{P_0 - {\beta_i, max}^2}, \tag{17}$$

where β_i, max denotes the maximum value of the incident waves (is always 1 because of the normalization). The first moment of the power delay profile is called *mean excess delay* $\overline{\tau_m}$ and provides information about how much the signal is spread in time-domain. It is calculated by applying

$$\overline{\tau_m} = \frac{\sum_i {\beta_i}^2 \tau_i}{\sum_i {\beta_i}^2}. \tag{18}$$

The square root of the second central moment of the PDP is called *RMS delay spread*. This parameter is important as it gives an approximation of the channel coherence bandwidth. The RMS delay spread τ_{rms} is given as

$$\tau_{rms} = \sqrt{\overline{\tau^2} - (\overline{\tau_m})^2} \tag{19}$$

with

$$\overline{\tau^2} = \frac{\sum_i {\beta_i}^2 {\tau_i}^2}{\sum_i {\beta_i}^2} \tag{20}$$

As mentioned above, the RMS delay spread gives an estimate for the channel coherence bandwidth. The coherence bandwidth is a statistical measure of the range of frequencies over which the channel passes all spectral components with approximately equal gain and linear phase. If we define the coherence bandwidth as the range where the channel's frequency transfer function has a correlation of at least 0.5, an approximation for the coherence bandwidth B_c is given as [5]

$$B_c \approx \frac{1}{5\tau_{rms}}. \tag{21}$$

2.2.3 Doppler spread

When transmitter and receiver move with respect to each other, in other words, if the distance between the two changes with time, another phenomenon becomes visible: the Doppler effect. To explain it, the case of a single sinusoidal wave with frequency f_c reaching the receiver is considered. It is also assumed that the receiver is moving away from the sender with constant speed v, so the distance between RX and TX is increasing. In this case, the frequency of the received oscillation is decreased by v/λ, in other words, the Doppler shift ν is given as

$$\nu = -\frac{v}{\lambda} = -f_c \cdot \frac{v}{c_a}, \tag{22}$$

where λ is the wavelength [7]. Assuming that the direction of the movement is not aligned with the direction of wave propagation we get

$$\nu = -\frac{v}{\lambda}\cos(\gamma) = -f_c \cdot \frac{v}{c_a}\cos(\gamma) = -\nu_{max} \cdot \cos(\gamma), \tag{23}$$

where γ denotes the angle between the direction of movement and the direction of wave propagation. The Doppler shift is negative when TX and RX move away from each other and positive in the opposite case. The Doppler shift is reciprocally proportional to the propagation speed of the wave, so for acoustic waves the resulting frequency shift is much greater in comparison to electromagnetic waves. Until now, only the behavior of one single incident wave has been discussed, in reality however, the incident wave will consist of the superposition of many MPCs with different Doppler shifts. This results in a broadening of the received spectrum, the so called Doppler spread. The Doppler spectrum is often mathematically modeled by the so called *Jakes spectrum* $S_c(\nu)$

$$S_c(\nu) = \frac{1}{\pi\sqrt{\nu^2{}_{max} - \nu^2}} \tag{24}$$

with the maximum Doppler shift

$$\nu_{max} = f_c \cdot \frac{v}{c_a}. \tag{25}$$

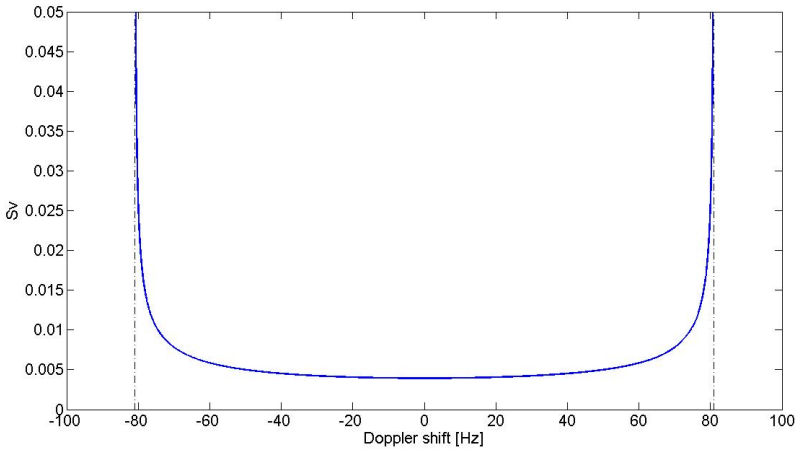

Figure 4: Jakes Doppler Power spectrum

Figure 4 shows the Jakes Doppler spectrum for the values f_c=20kHz, $v = 1.39m/s$ and c_a=343m/s. It has to be noted that the shown spectral shape is a result of a dense-scatterer channel model. For indoor channel models a flat spectrum is assumed [11]. The Doppler spectrum has two important interpretations [7]:

1. It describes frequency dispersion which can lead to transmission errors and
2. it is a measure for the temporal variability of the channel (as the different shifted MPCs will cause fading dips because of destructive interference).

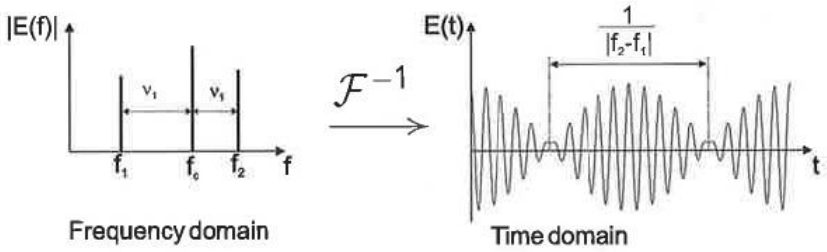

Figure 5: Superposition of two carriers with different frequencies (beating) [7]

Figure 5 shows the principal effect for the superposition of two simply Doppler-shifted sinewaves (no more multipath components), the interference of the two waves causes fading dips, also called beatings. The period of time T_p between two consecutive dips is inversely reciprocal to the difference of the frequencies of the waves and given as

$$T_p = \frac{1}{\mid f_2 - f_1 \mid}. \tag{26}$$

Although the example in Figure 5 is a very simple one, it shows that the fading rate of a channel is related to the Doppler shift, or, in a scenario with many multipath components, the Doppler spread.
A very useful channel parameter is the so called coherence time, the time span in which the channel can be assumed to be approximately constant. An estimate for the coherence time T_c is the reciprocal of the RMS Doppler spread and is given as

$$T_c \approx \frac{1}{\nu_{rms}}. \tag{27}$$

The RMS Doppler spread can be calculated by applying

$$\nu_{rms} = \sqrt{\overline{\nu^2} - \bar{\nu}^2} \tag{28}$$

with the first moment of the Doppler spectrum $\bar{\nu}$

$$\bar{\nu} = \frac{\int_{-\infty}^{\infty} \nu \cdot S_c(\nu) d\nu}{\int_{-\infty}^{\infty} S_c(\nu) d\nu} \tag{29}$$

and the second moment $\overline{\nu^2}$ which is defined as

$$\overline{\nu^2} = \frac{\int_{-\infty}^{\infty} \nu^2 \cdot S_c(\nu) d\nu}{\int_{-\infty}^{\infty} S_c(\nu) d\nu}. \tag{30}$$

3 Channel measurements

In order to identify the channel, to extract the channel parameters described in 2.2.2 and furthermore to be able to design a transmission scheme for this channel, it was indispensable to *sound* the channel first. The term *channel sounding* refers to the process of measuring the properties (namely the channel impulse responses, CIR) of the channel. Moreover, as mentioned before, for this specific channel there were no channel models at hand. Disposing of the measured data provided the opportunity to implement a channel model so that there was no need to work with the real, physical indoor channel again from that point on. Another advantage due to this decision was that simulations could be repeated easily (better reproducibility). This chapter is devoted to the measuring process of the CIR as well as the extraction and calculation of the channel parameters. Furthermore, some interesting channel behavior aspects in time domain will be shown.

3.1 Identifiability of the channel

According to [7], a time-invariant channel can always be identified by appropriate measurement methods if only the receiver fulfills the Nyquist theorem in the delay domain, i.e., samples the received signal sufficiently fast. For a time-variant channel the situation is a bit more complicated as the channel model has to track the changes in the channel. A measured impulse response at a given position is referred to as a "snapshot". These snapshots have to be taken sufficiently often in order to get an aliasing-free measurement. Analogously to the sampling theorem for band-limited signals there is a minimum temporal sampling rate f_{rep} to identify a time-variant process with a band-limited Doppler spectrum. The sampling rate has to be at least twice the maximum Doppler frequency ν_{max} and therefore has to be

$$f_{rep} \geq 2\nu_{max}. \tag{31}$$

Using the relation

$$\nu_{max} = \frac{f_{max} v_{max}}{c} \tag{32}$$

where f_{max} denotes the (maximum) frequency of the transmitted signal, v_{max} the maximum speed of movement and c the propagation speed of the signal, the repetition time interval of the snapshots can be written as

$$T_{rep} \leq \frac{c}{2 f_{max} v_{max}} \tag{33}$$

using

$$T_{rep} = \frac{v}{\triangle x_s}, \tag{34}$$

where v denotes the speed of movement and $\triangle x_s$ the distance between the locations at which the sounding takes place. Combining (33) and (34) we obtain

$$\frac{v}{\triangle x_s} \geq 2\frac{v_{max}}{\lambda} \tag{35}$$

and rewriting (35) brings us to

$$\triangle x_s \leq \frac{v}{v_{max}} \frac{\lambda}{2} \leq \frac{\lambda}{2}. \tag{36}$$

Considering (35), the distance $\triangle x_s$ must be smaller than half of the wavelength of the highest frequency. As the highest frequency of the acoustic communication system is 20kHz, the minimum wavelength λ_{min} is calculated as

$$\lambda_{min} = \frac{c}{f_{max}} = \frac{343m/s}{20kHz} = 17.15mm \tag{37}$$

which leads to a maximum distance between two consecutive screenshots of

$$\triangle x_{s,max} = \frac{\lambda_{min}}{2} = 8.575mm. \tag{38}$$

For the channel sounding the distance was chosen to be $\triangle x_{s,meas} = 5mm$.

3.1.1 Maximum length sequences

In order to measure the channel, maximum length sequences (MLS) can be used [8]. An MLS is a periodic, pseudo-random binary signal of length $L = 2^m - 1$, where m denotes the order of the sequence and L the periodicity. Maximum length sequences have a number of attractive properties. The most important one is that the autocorrelation function of the sequence is a perfect impulse except for a small DC error. In general, MLS share many statistical properties with white noise despite being completely deterministic. They have, except for values very close to zero, a constant frequency spectrum, which is shown in Figure 6. These sequences can be generated easily by using shift-registers. By assigning the physical values +1 and -1 to the logical values 0 and 1, an RMS-value of 1 (which is also the maximum magnitude of the signal) is obtained. Figure 7 shows a small section of such a sequence and Figure 8 the corresponding autocorrelation function.
In order to measure the impulse response of a linear system, the MLS signal is applied to the system. The system response is measured and crosscorrelated with the known MLS. The result is the periodic impulse response of the system.

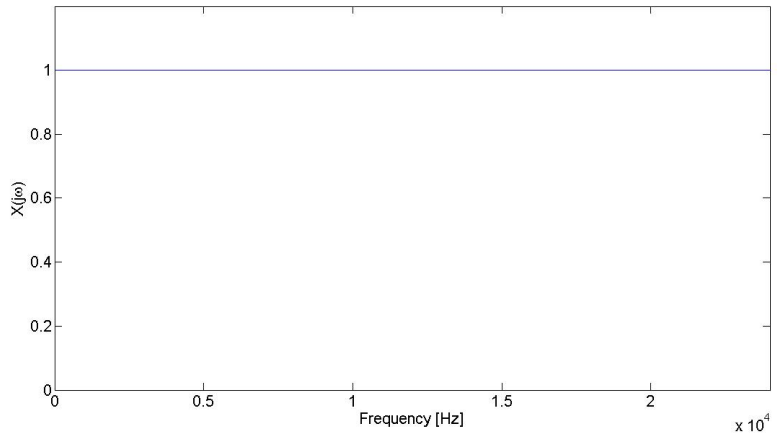

Figure 6: Spectrum of a MLS

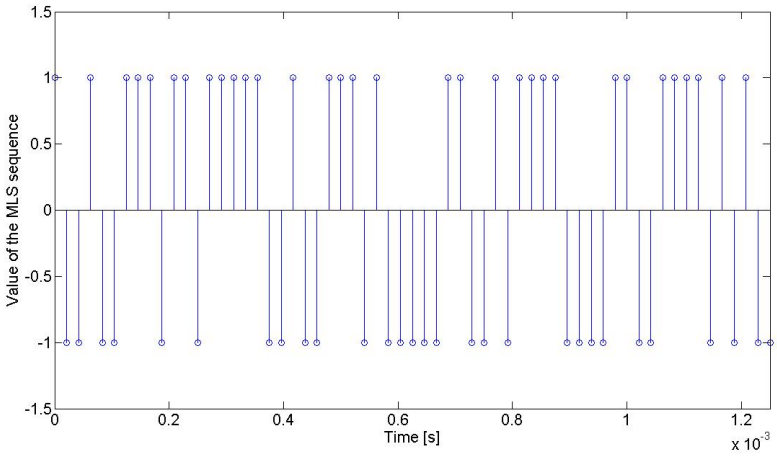

Figure 7: Section of a MLS

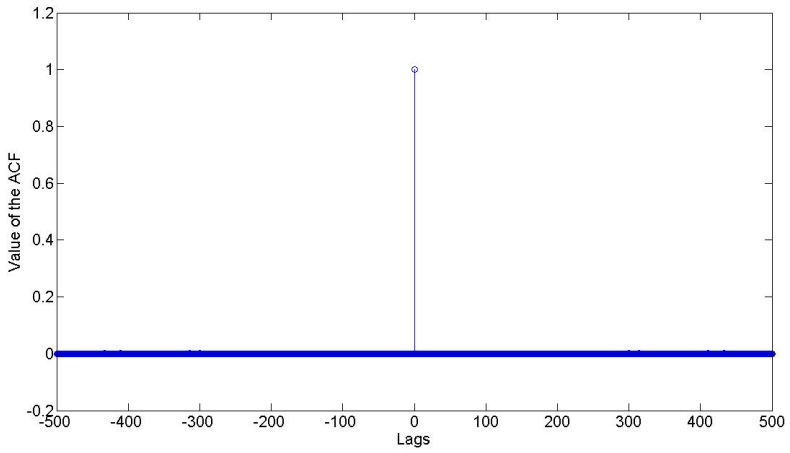

Figure 8: Autocorrelation function of a MLS

The period of the MLS is given as

$$T_{MLS} = \frac{L}{f_s}, \tag{39}$$

where L is the length of the sequence and f_s is the sampling frequency. The length also determines the frequency resolution $\triangle f$ of the measurement as

$$\triangle f = \frac{1}{T_{MLS}} = \frac{f_s}{L}. \tag{40}$$

The period has to be chosen sufficiently large in order to prevent that the transients from previous periods interfere with the actual one (time-aliasing), so the period should be clearly bigger than the maximum excess delay of our channel. From very basic measurements regarding the excess delay of the channel it is known that a sequence of an order of m=15 with a period of $T_{MLS} = 0.683s$ will be sufficient.

Principles of the MLS measurement

MLS methods necessarily measure the periodic impulse response (PIR) and not the true, linear impulse response of a linear system (IR). When characterizing a linear system under periodic convolution by its periodic impulse response denoted by $h'[n]$, the periodic output $y'[n]$ is given by periodic convolution of a periodic input $x'[n]$ with $h'[n]$. The following closely follows [8]:

$$y'[n] = x'[n] \star h'[n] \tag{41}$$

$$= \sum_{k=0}^{L-1} x'[k]h'[n-k]. \tag{42}$$

Note that the index $n-k$ is evaluated modulo L and $x'[n]$, $h'[n]$ and $y'[n]$ are all periodic sequences with period L. From this point on, all index arithmetic for periodic sequences is modulo L unless otherwise denoted. The relationship between the IR and the PIR is given by

$$h'[n] = \sum_{k=-\infty}^{\infty} \delta'[k]h[n-k] \tag{43}$$

$$= \sum_{k=-\infty}^{\infty} h[n+kL]. \tag{44}$$

In the previous subsection it was mentioned that the period of the MLS was chosen sufficiently long so that the impulse response $h[n]$ decays to a negligible value during L samples, so time-aliasing is avoided. Therefore, the periodic impulse response $h'[n]$ closely approximates the first L samples of the linear impulse response. As mentioned before, the periodic autocorrelation function $\phi'_{xx}[n]$ of an MLS is essentially a periodic unit-sample sequence given as

$$\phi'_{xx}[n] = x'[n] \otimes x'[n] \tag{45}$$

$$= \frac{1}{L}\sum_{k=0}^{L-1} x'[k]x'[k+n], \tag{46}$$

wher

$$\phi'_{xx}[n] = \begin{cases} 1, & n = 0 \\ -\frac{1}{L}, & 0 < n < L \end{cases} \tag{47}$$

For convenience in the analysis, the autocorrelation is normalized by $L+1$ instead of the usual factor L as shown in (46). This renormalization results in a slightly different expression for the autocorrelation function, now denoted as Ω'_{xx}, given by

$$\Omega'_{xx}[n] = \frac{1}{L+1}\sum_{k=0}^{L-1} x'[k]x'[k+n] \tag{48}$$

with

$$\Omega'_{xx}[n] = \begin{cases} \frac{L}{L+1}, & n = 0 \\ -\frac{1}{L+1}, & 0 < n < L \end{cases} \tag{49}$$

The expression from (49) can be rewritten to

$$\Omega_{xx}{}'[n] = \delta'[n] - \frac{1}{L+1} \tag{50}$$

To obtain the imulse response of the system, the MLS sequence $x'[n]$ will be crosscorrelated with the system response $y'[n]$ given as

$$\Omega'_{xy} = \frac{1}{L+1}\sum_{k=0}^{L-1} x'[k] \cdot y'[k+n]. \tag{51}$$

With $\otimes$ as the cross-correlation operator we get

$$\begin{aligned} \Omega'_{xy} &= x'[n] \otimes y'[n] && (52)\\ &= x'[n] \otimes \{x'[n] \star h'[n]\} && (53)\\ &= \{x'[n] \otimes x'[n]\} \star h'[n] && (54)\\ &= \Omega'_{xx} \star h'[n]. && (55) \end{aligned}$$

The periodic cross-correlation of in- and output signal is equivalent to the convolution of the autocorrelation function of the MLS with the periodic impulse response. Substituting (50) into (55) gives

$$\begin{aligned} \Omega'_{xy}[n] &= \{\delta'[n] - \frac{1}{L+1}\} \star h'[n] && (56)\\ \Omega'_{xy}[n] &= h'[n] - \frac{1}{L+1} \sum_{k=0}^{L-1} h'[k]. && (57) \end{aligned}$$

In (57) it becomes visible that the result of the cross-correlation contains the periodic impulse response $h'[n]$ and a constant component. For big values of L, the constant component is strongly suppressed and the approximation

$$\Omega'_{xy}[n] \approx h'[n] \tag{58}$$

is valid. The result of the cross-correlation of a MLS with the corresponding periodic system response is the periodic impulse response of the system. The MLS necessarily measures the periodic impulse response and not the true response. However, when applied to a real system, circular convolution cannot be achieved as real systems apply linear convolution, with an unexcited initial state. Circular convolution may be approximated by stimulating the system with the MLS sequence twice and analyzing the second sequence. It has to be noted that the measured impulse response is not purely the impulse response of the channel but furthermore also includes the used sender and receiver hardware (in other words, the channel model contains the transfer functions of the soundcard of the used computer, speaker, microphone, amplifiers, etc.).

3.2 Scenario setup

The following will give an overview of the physical indoor channel which should be sounded. In a room, as shown in Figure 9, a speaker, the sender, is positioned at a fixed point while the receiver, a microphone, moves from its initial point 1.5m away from the TX along a 2m trajectory until the final position (at a distance of 3.5m to the transmitter).

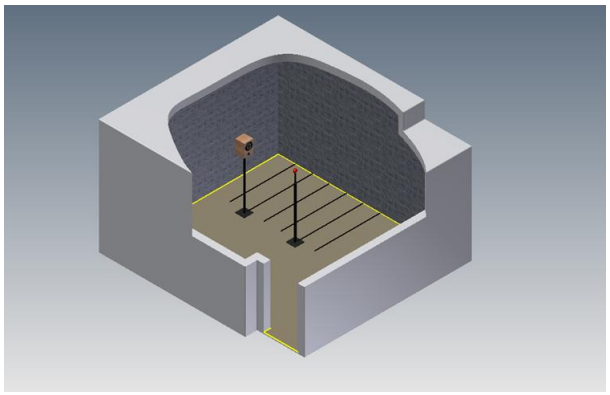

Figure 9: Schematic illustration of the room (3D).

Additionally, we distinguish between a line-of-sight (LOS) scenario (Figure 10) and a non-line-of-sight (NLOS) one. In the NLOS case (Figure 11), the speaker will be rotated so that there is no intentional direct path between sender and receiver and all the incident waves arrive at the RX after being reflected at least one time. (The main direction of propagation of the transmitter is indicated by an arrow on the speaker symbol.) The movement of the receiver is the same for both scenarios. The CIRs along this trajectory were measured using the MLS method described in Section 3.1.1. As mentioned in Section 3.1, the distance between two consecutive MLS measurements was chosen to be 5mm, which leads to $\frac{2m}{5 \cdot 10^{-3} m}$=400 snapshots for each scenario. Illustrations of the process of the measurements including the description of the used software can be found in Appendix A.1.

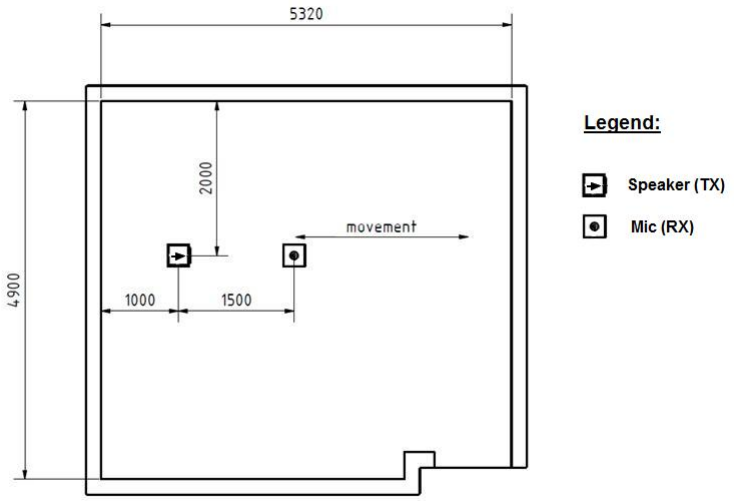

Figure 10: System setup of the LOS measurements (distances are given in mm)

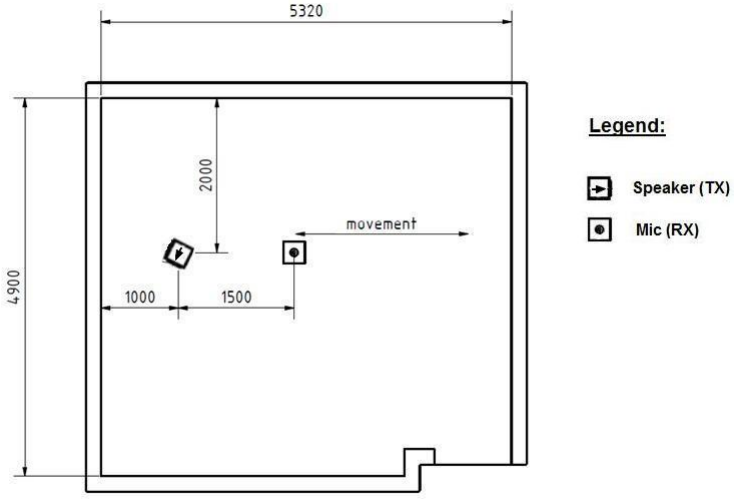

Figure 11: System setup of the NLOS measurements (distances are given in mm)

3.3 Channel parameter evaluation

In this subsection the results of the measurements made in 3.2 are presented. First, impulse responses from different positions and scenarios are shown. In Section 2.2.2 some important channel parameters and the way how to calculate them based on the APDP were presented. The obtained APDPs for the LOS and the NLOS scenario are presented in 3.3.2 and the formulas for extracting the channel parameters described before will be applied in order to obtain the values of the channel parameters. Then, in 3.3.3, Doppler Power Spectra in different frequency ranges are obtained and the corresponding RMS Doppler spreads are calculated for LOS and NLOS.

3.3.1 LOS and NLOS

The Figures 12-15 show some examples of measured channel impulse responses. The first two Figures are taken from the LOS scenario whereas the second two are obtained from the NLOS type. In both scenarios a highly time-dispersive channel behaviour becomes evident. A signal sent over this channel will be heavily distorted. From the measured CIR it can be seen that for the LOS scenario the first arriving component is the strongest. All the other components of the incident wave suffer higher attenuation due to higher free-space and reflection losses. If there is no direct path between sender and receiver (NLOS), the first arriving component isn't neccessarily the strongest one. It becomes also evident that the signal is spread even more in time-domain and no dominant component is visible. Comparing Figure 12 and 13 (also 14 and 15), also the time-offset caused by the greater distance between sender and receiver can be seen. In the LOS case, the first arriving component also gets less dominant as it undergoes stronger attenuation due to the free-space loss.

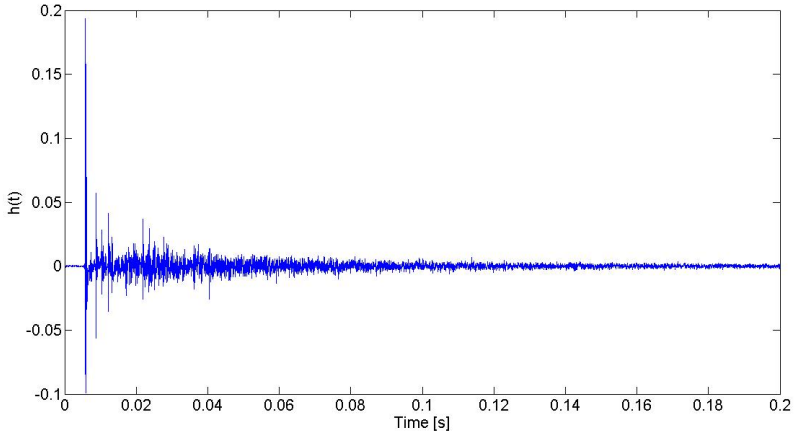

Figure 12: CIR, LOS scenario, 1.5m distance

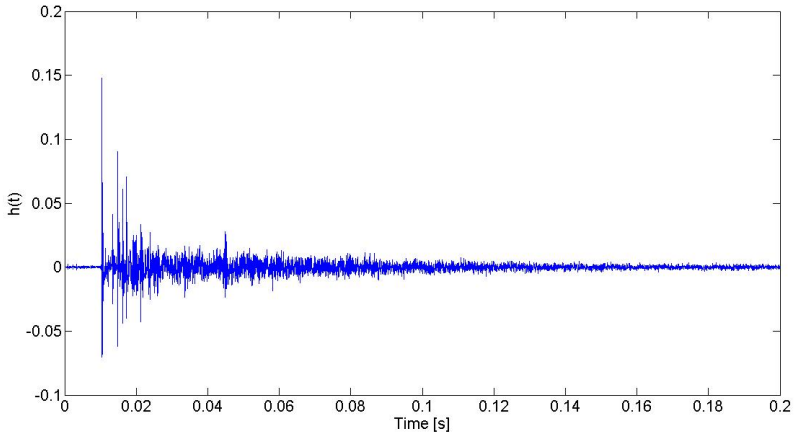

Figure 13: CIR, LOS scenario, 3.1m distance

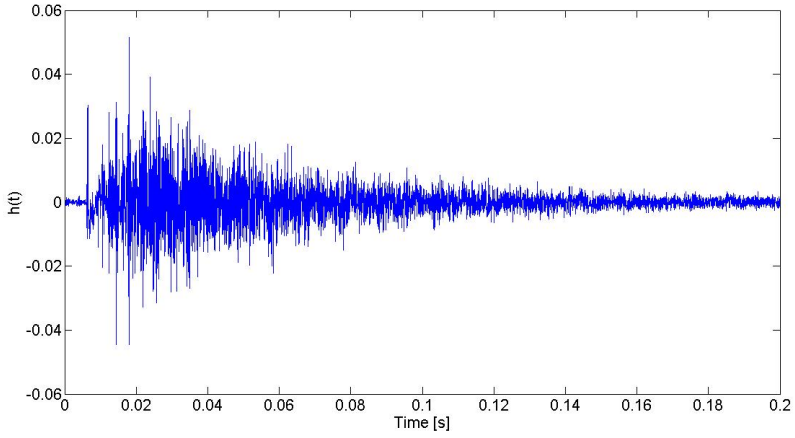

Figure 14: CIR, NLOS scenario, 1.5m distance

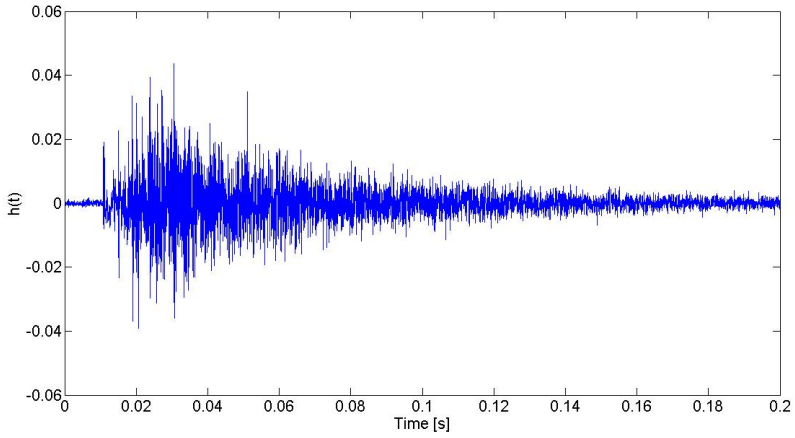

Figure 15: CIR, NLOS scenario, 3.1m distance

3.3.2 APDP, delay spread & K-factor

The Figures 16 and 17 show the Average Power Delay Profiles for the LOS and the NLOS case respectively. In the LOS scenario the first arriving component is, as expected, by far the strongest one. All other incident waves exhibit (on average) a power level about 15dB below the one of the dominant component. After about 230ms, the level of the signal falls below the noise floor and disappears. In the NLOS case we see again that the signal is spread more in time domain, the maximum power is located at about 20ms after the first wave detection. The maximum excess delay is about 300ms.

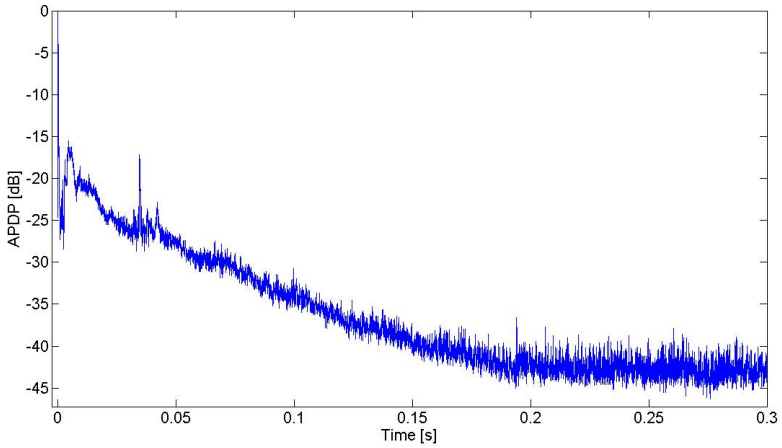

Figure 16: Average Power Delay Profile, LOS scenario

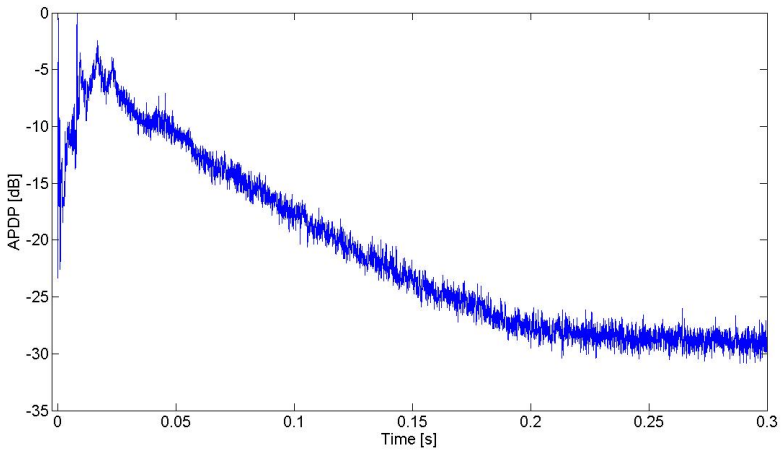

Figure 17: Average Power Delay Profile, NLOS scenario

Table 2 shows the extracted parameters for the LOS and the NLOS scenario applying the formulas for the channel parameters in 2.2.2.

Scenario	P_0 [dB]	K_{LOS}	$\overline{\tau_m}$ [ms]	τ_{rms} [ms]	B_c [Hz]
LOS	4.79	0.496	20.8	33.9	5.9
NLOS	17.84	0.016	39.6	39.4	5.1

Table 2: Channel parameters for the LOS and NLOS scenario

The fact that the K-factor in the LOS case is much bigger as in for the NLOS scenario is conform with the observations made before. A big amount of the transmitted energy is located in the first arriving wave, the dominant component, whereas for the scenario without dominant component the energy is spread more. It has to be noted that in the NLOS case there was not more energy received as in the LOS scenario, although Table 2 indicates it. This result is a consequence of the normalization of the APDP, where the value of strongest incident wave had been set to one. Hence, as the signal shows a bigger delay spread, more energy is detected. The values of the RMS Delay Spread are $\tau_{rms,LOS}$=33.9ms for LOS and estimates for $\tau_{rms,NLOS}$=39.4ms for NLOS, leading to the (estimated) channel coherence bandwiths of $B_{c,LOS}$ ≈5.9Hz and $B_{c,NLOS}$ ≈5.1Hz, respectively.

3.3.3 Doppler spread

It was already discussed that a relative movement between TX and RX causes a frequency shift of the transmitted signals due to the Doppler effect, and, in the case of the presence of MPC, a spectral broadening. In order to study

this resulting spectral broadening of the given acoustic channel, a test signal, a complex sinusoidal was sent over the implemented channel model from 2.2, where the channel impulse matrix **H** was filled with the measured CIR (the implementation of channel model will be discussed in more detail in chapter 3.7) . Mathematically, the sent signal $x(t)$ can be expressed as

$$x(t) = A \cdot e^{j2\pi f_c t},$$

where A denotes the peak value of the signal and f_c its frequency. This *analytic signal* has no negative frequency components, so the spectrum consists of only one single spectral line at the given frequency f_c. In the following, the spectra of the received signals in LOS and NLOS scenario (assuming a velocity of a 1.39m/s between TX and RX) for different values of f_c are shown.

f=1kHz (LOS):

The corresponding spectra are shown in Figure 18. The spectrum of the sent signal shows only one peak at exactly 1kHz, meanwhile the influence of the channel is visible when observing the spectrum of the received signal. This signal shows components apart from the original one, which is caused by the Doppler spread.

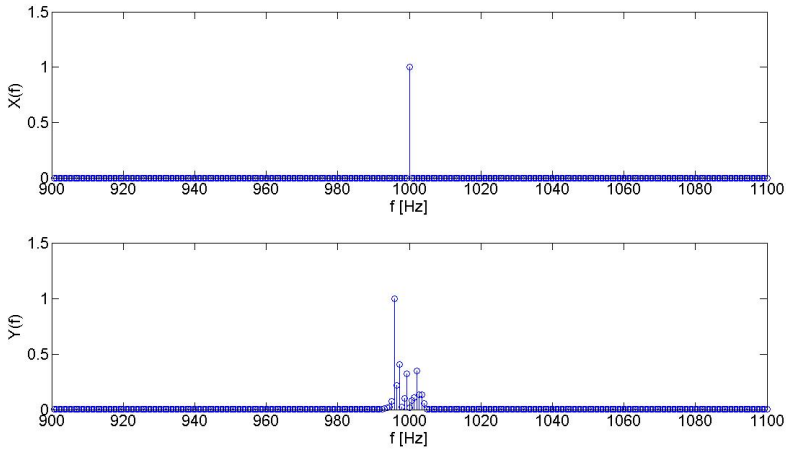

Figure 18: Spectra of sent and received 1kHz signal

Figure 19 shows this spectrum in more detail. Recalling (23) and (25) and taking in account that the angle between the movement of the receiver and the main direction of wave propagation is zero (for the LOS scenario this is true) we calculate the theoretical maximum Doppler spread to be $v_{max} = 4.05$Hz, which corresponds to the measured value of the strongest peak in the spectrum (the theoretical maximum value is indicated by the black, dashed line in the

illustration). This peak at about 996Hz corresponds to the LOS component which is simply shifted down in frequency because the RX moved constantly away from the TX. The other peaks show MPC arriving at different angles after being reflected. Therefore, some incident waves reached the receiver against its movement direction and were shifted towards higher frequencies as a consequence. Considering the fact that they were reflected and traveled a longer distance before arriving at the RX, it seems logical that they are clearly weaker as the dominant component.

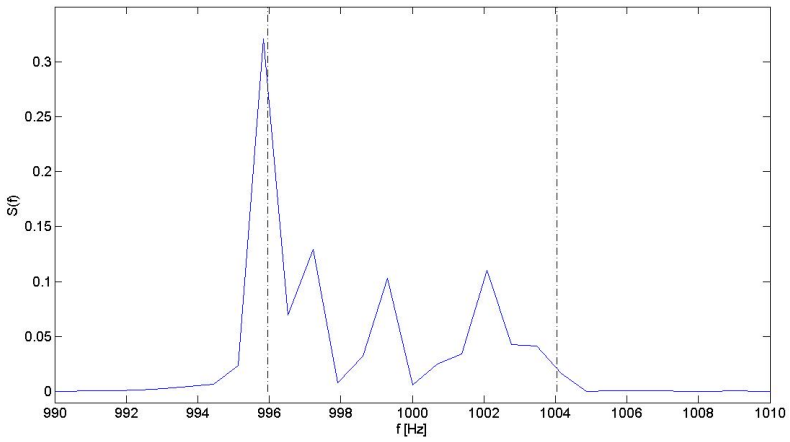

Figure 19: Spectrum of received 1kHz-signal; Doppler Power Spectrum

f=20kHz (LOS):

Again, a complex sinusoidal was sent over the channel of the LOS scenario, this time with a frequency of 20kHz. Again, the spectrum of the sent signal consists in only one spectral line, without presence of negative frequency components. The theoretical maximum Doppler shift for a 20kHz-sinewave is 80.99Hz. Figure 20 shows the measured spectrum.

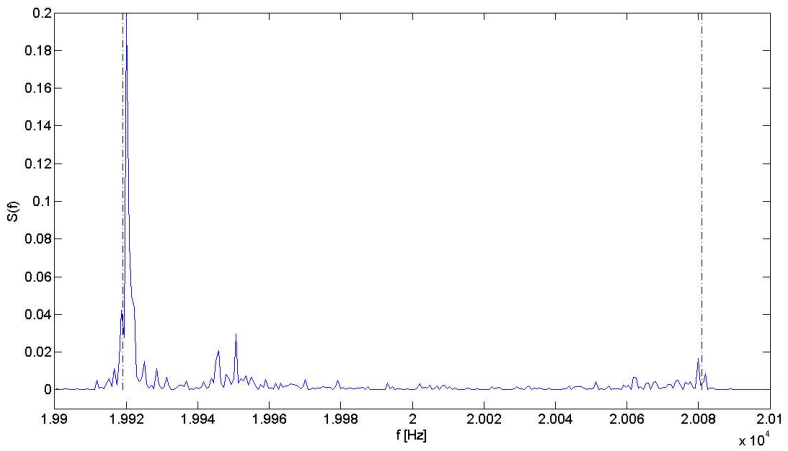

Figure 20: Spectrum of received 20kHz-signal; Doppler Power Spectrum

With this higher-frequent sinusoidal it becomes even more evident that the line of sight-component is very dominant as the Doppler shift for this frequency values is much bigger and the different MPC are dispersed much more in frequency domain, depending on their arrival angle. Hence, they are easily distinguisable where in the case of the 1kHz sinewave they apparently overlap each other. The resulting spectrum shows again one strong peak at the expected position of $-v_{max}$, which correspond to the direct arriving wave. Again, the obtained value coincides with the theoretical one.

f=1kHz (NLOS):

Until this point, the LOS channel scenario was used for the simulation, now the impact of the NLOS scenario on the signals will be examined. The same complex 1kHz-sinewave as before was sent over the channel.

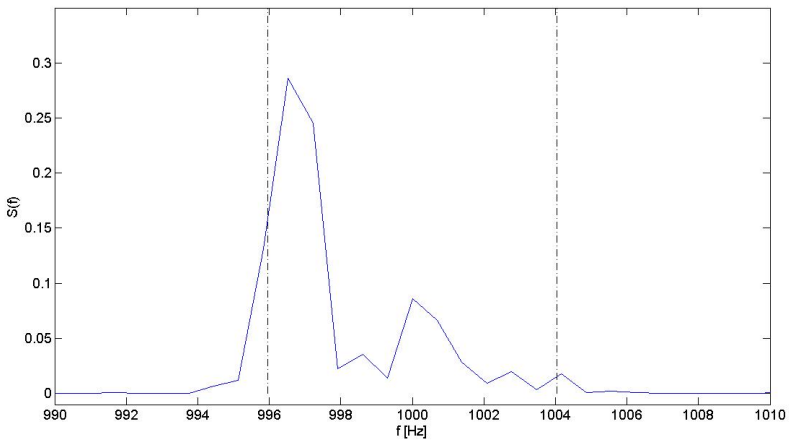

Figure 21: Spectrum of received 1kHz-signal; Doppler Power Spectrum

In the NLOS case the Doppler spectrum does not seem so different in comparison to the LOS scenario. Again, most of the signal power is concentrated towards lower frequencies w.r.t. the center frequency of 1kHz. Nonetheless, this time the peak is located at a frequency shift that is smaller than the theoretical maximum value of v_{max} =4.05Hz. Also, the peak appears to be thicker than in the LOS case which indicates the superposition of more MPC arriving at a similar angle.

f=20kHz (NLOS):

One more time the complex 20kHz-sinusoidal was used for testing reasons in the NLOS scenario.

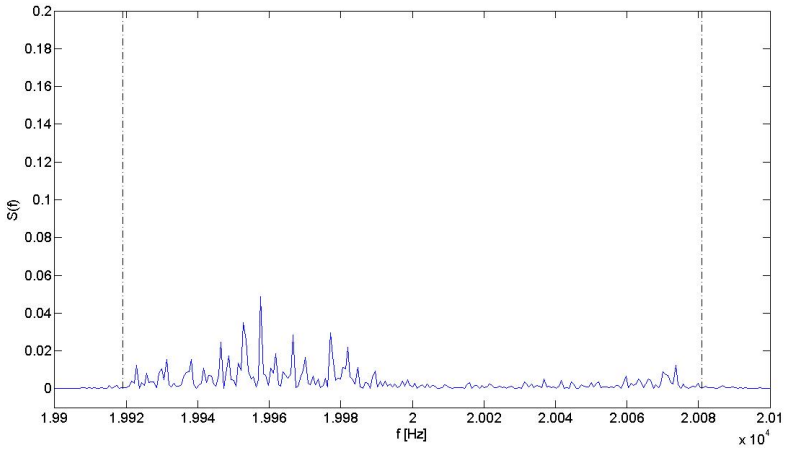

Figure 22: Spectrum of received 1kHz-signal; Doppler Power Spectrum

The spectrum again has a span of approximately ±80Hz, but this time the components with the maximum shift are not the strongest ones, in fact, the most energy is found about ±40Hz around the center frequency which indicates that most waves arrive at an angle of about 45° w.r.t. the movement of the RX. Obviously the arriving waves do not arrive uniformly distributed as assumed in the deduction of the theoretic Jakes Doppler Spectrum which leads to a very differently shaped spectrum.

Calculation of the Channel Coherence Time:

Applying (29), (30) and (28), the values of the RMS Doppler spread for the LOS and the NLOS scenarios were calculated. Moreover, an estimate for the channel coherence time can be obtained by applying (27). Table 3 shows the calculated values. Looking at the Figures 20 and 22, one might expect a higher

Scenario	ν_{rms} [Hz]	T_c [ms]
LOS	51.7	19.4
NLOS	43.3	23.1

Table 3: Obtained values for RMS Delay Spread and Channel Coherence Time

RMS Doppler spread in the NLOS scenario because the signal energy is spread more in frequency domain. In the LOS case, the dominant component, which

contains the most energy, is shifted to the theoretical maximum shift value, but less spreading takes place. Nonetheless, the value of the RMS Doppler spread is bigger in the LOS. This can be explained remembering the definition of the RMS Doppler spread given in (28), and especially the definition of the second moment in (30). For high values of the shift, the second moment takes an even greater value and therefore also the resulting RMS Doppler shift is bigger than in the NLOS case, where more frequency-shifted components are visible, but with lower shift values.

3.4 Channel Transfer Function

After having obtained some insight into the narrowband behavior of the channel, this subsection will focus on obtaining the channel transfer function (CTF) in order to investigate the behavior of the channel over the whole bandwith. The transfer function is both frequency and time dependent, so $H = H(t, \omega)$. The Fourier transform of a channel impulse response gives the CTF. In order to obtain an average channel transfer function, all the measured IRs were Fourier transformed, the results correspond to the CTF at the measured points along the trajectory. The arithmetic mean of all the CTF amplitudes gives the average channel transfer function $H_{av}(\omega)$. The Figures 23 and 24 show these average channel transfer functions for LOS and NLOS scenario.

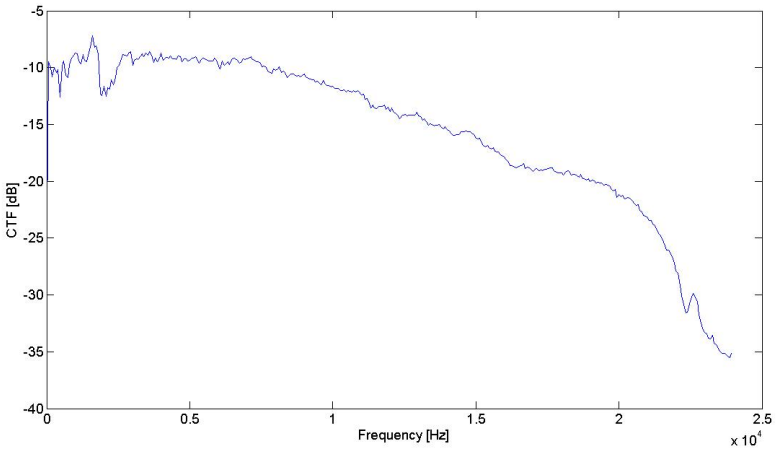

Figure 23: Channel transfer function (CTF) for the LOS case

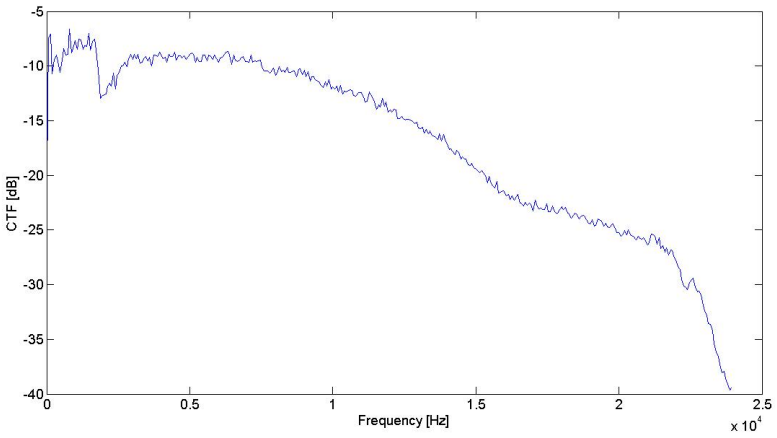

Figure 24: Channel transfer function (CTF) for the NLOS case

In both cases, the channel shows strong lowpass behavior, leading to attenuate high-frequent components way stronger than the ones with lower frequency. It also shows a bigger attenuation for signals of around 2 - 2.5kHz. This has to be considered when implementing a transmission system for this channel. Signals in some frequency bands either have to be sent with higher power or be amplified at the receiver side. The behavior is very similar in both cases, so apparently the physical channel itself, the space between sender and receiver, seems not to be the reason for these effects. Also, the attenuation is way bigger than could be explained by the frequency-dependent free-space-loss. The reason was found in the fact that, as mentioned, the measured channel model does not only include the physical channel but furthermore also the transfer functions of transmitter and receiver. As they are part of what is called the channel, this fact has to be accepted and its influence to be compensated when implementing a data transmission.

3.5 Subcarrier Impulse Responses

In Section 3.3.1, various impulse responses (both for the LOS and the NLOS scenario) were shown. These measured IRs consist of frequency components of the whole spectrum (up to half the sample frequency). An interesting question is if there is a frequency dependence of the impulse responses. In other words, do lower frequency components of an IR decay faster than the higher ones, or vice versa? In order to answer this question, for the impulse responses shown in Figure 12 and 14, different frequency bands (spectral components) of the IR were extracted. In the following, the IR for one specific frequency band will be denoted as *subcarrier impulse response*. The process of extracting one of these subcarrier IRs is depicted in Figure 25.

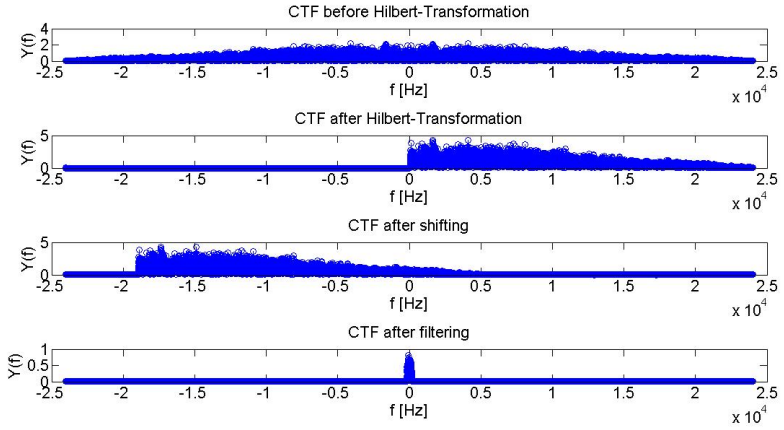

Figure 25: Spectrum of an IR during the extraction of the subcarrier IR

The spectrum of the original IR is shown in the first illustration in the figure. In the first step, the impulse response is converted into an analytic signal by performing the Hilbert transform. The resulting signal does not have any negative frequency components, as shown in the second illustration. Then, by applying the frequency shift theorem [6]

$$e^{j\omega_0 n}x[n] \longleftrightarrow X(e^{j(\omega-\omega_0)}) \tag{59}$$

the analytic signal is shifted down by a certain frequency ω_0 (19kHz in the illustration) in frequency domain, shown in the next image. Finally, the frequency shifted (analytic) impulse response is filtered by a low-pass with a cut-off frequency of 60Hz. Therefore, the resulting signal corresponds to the impulse response of an carrier at ω_0 with a bandwidth of $\pm$60Hz. The spectrum of this resulting subcarrier impulse response is shown in the last illustration. The so obtained subcarrier IRs for frequencies of 300Hz and 19kHz are shown in Figure 26, where the difference becomes clearly visible. The IR of the 300Hz carrier decays much slower than the one with 19kHz. In the second case, after 25ms the signal's level already drops below a quarter of the inital value whereas for the lower frequency carrier this happens at about 150ms.

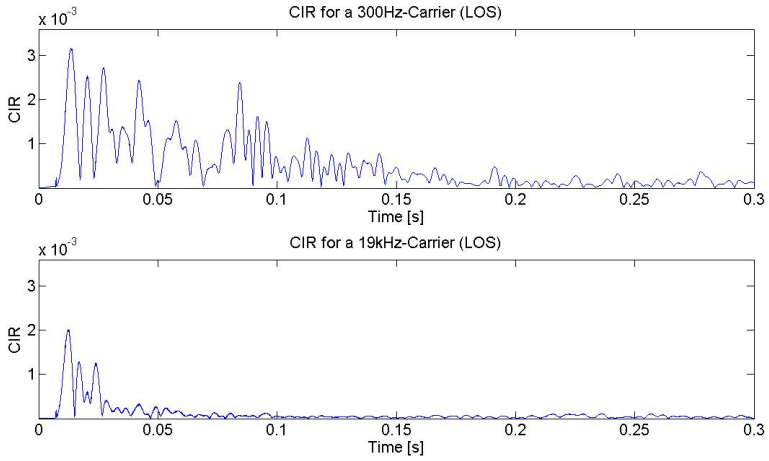

Figure 26: Subcarrier IR for 300Hz and 19kHz (LOS)

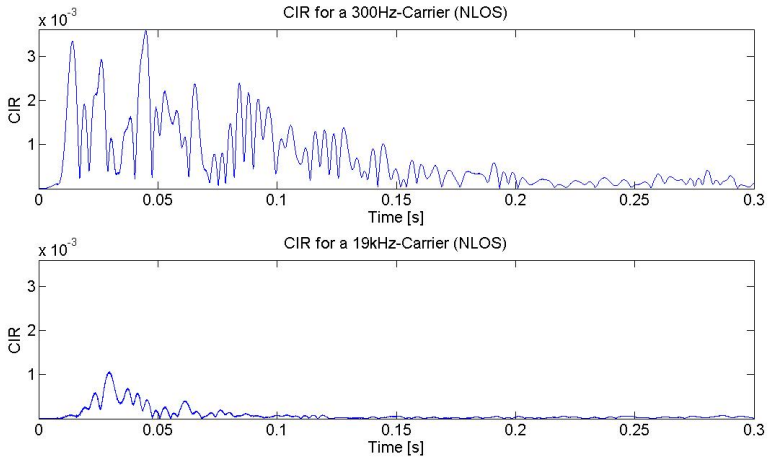

Figure 27: Subcarrier IR for 300Hz and 19kHz (NLOS)

The obtained IRs in the NLOS scenario show the same behavior, high frequent multipath components are much more attenuated when being reflected on their way to the receiver, resulting in a much faster decaying (subcarrier) impulse response. This could be used by implementing a transmission scheme in which different symbol rates on different carriers are used. Due to the faster decaying impulse responses, high frequent carriers could use smaller intervalls between subsequent symbols in order to increase the obtainable data rate without causing greater ISI and a higher bit error rate.

3.6 Time-variability of the channel

As explained in Section 2.2.3, the time-variability of a channel is related to the Doppler spread because of the interfering, frequency-shifted multipath components. This section focusses on these variations due to the Doppler spread by observing the envelopes of the received sinusoidal signals from Section 3.3.3. It has to be noted that therefore the variations are not equivalent to the time-variant channel transfer function $H(t, f)$, they show only the time-variability of the channel at the specific frequencies of the sent sinusoidal signals, namely 1kHz and 20kHz, respectively. Figure 28 shows $H(t, 1\text{kHz})$ for the LOS scenario. As the envelope of the sent signal was constant and equal to one, the received signal shows the channel transfer function at a frequency of 1kHz as a function of time, $H(t, 1\text{kHz})$.

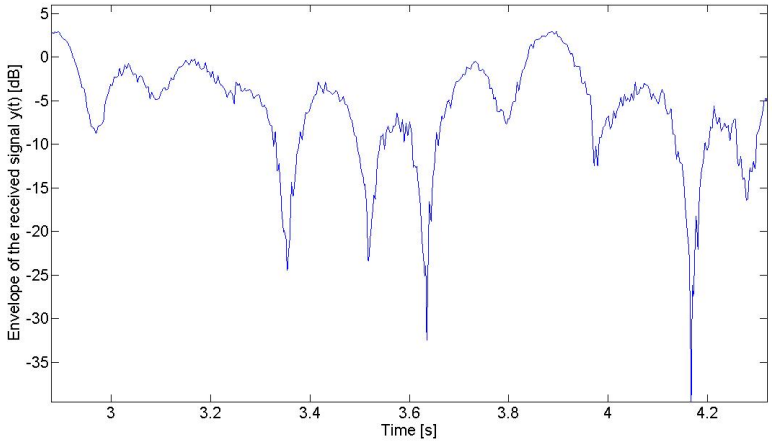

Figure 28: Time-variability of the channel at 1kHz (LOS)

Figure 28 shows a section of $H(t, 1\text{kHz})$. Note that the y-axis is shown in dB-scale. The time-variant nature becomes clearly visible, exhibiting fading dips down to values of -40dB. An interesting phenomenon can be observed regarding the fading dips: although they vary strongly with respect to their depth, they seem to occur with a certain periodicity. Note that although the term periodicity is used, it does not refer to the meaning of the word in the strict sense, a strictly periodic occurence with fixed intervall, but to a certain notable, fundamental repetition frequency that varies between 100 and 200ms. This can be explained when taking in account the corresponding Doppler spectra from Figure 19 and the theory of a two-path model shown in Figure 5. The Doppler spectra show only a few peaks with a maximum frequency shift of 6Hz. Taking (26) in account, the superposition of only two frequency-shifted separated by 6Hz would lead to a fading dip frequency of 1/6Hz=167ms. However, in the measured case, there are more frequency components existent, and therefore

the time between two consecutive dips varies as well as their depth. With rising signal frequency, the Doppler spread increases linearly and thus, also the fading dip frequency is much higher. This can be seen in Figure 29, where the transfer function for the NLOS scenario at a frequency of 20kHz, $H(t, 20\text{kHz})$, is shown. The fast-varying nature of the channel becomes evident, also the fading dips seem to occur more randomly. Again, the explanation for this behavior can be obtained from the Doppler spetrum (Figure 22). In this case without dominant component, many signal components with different frequency shifts are interfering and cause a more complex fading behavior. Also the already investigated lowpass behavior of the channel can be seen from the much lower average received power.

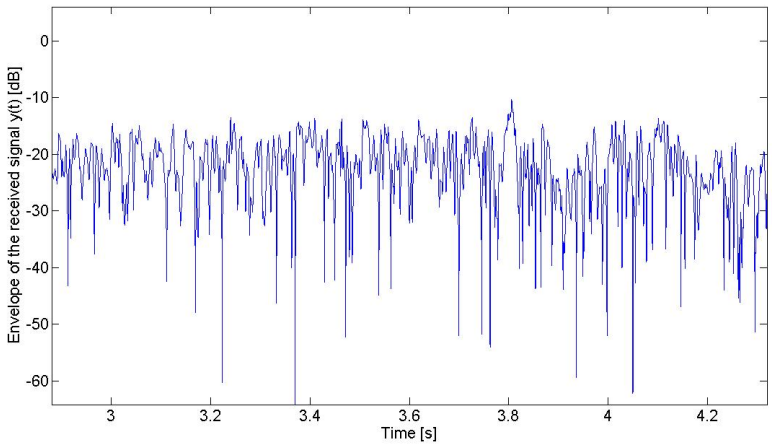

Figure 29: Time-variability of the channel at 20kHz (NLOS)

It has to be noted that already the transfer function with the least time-variant behavior, $H(t, 1kHz)$ for the LOS case, shows fading dips down to values of -40dB with a duration of about 50-60ms. Regardless of the implemented modulation scheme, transmitted symbols during this time span are corrupted severely.

3.7 Simulation framework

In this section, the implementation of the mathematical channel model from Section 2.2 in MATLAB will be explained. As shown there, recalling (13), the impact of the channel on the transmitted signal can be described as the convolution of the sent signal $x[n]$ with the channel impulse response $h_n[n]$ at the corresponding time instance. There, the channel impulse response matrix $\underline{H}$ was introduced. Each row of the impulse response matrix corresponds to the IR at the corresponding time instance. This time-variant filter model was

implemented in MATLAB in order to model the channel.

3.7.1 Interpolation between the measured CIR

It has to be noted that in order to obtain an exact model, one measured channel impulse response for every time instance n would be needed, so for a sampling rate of 48kHz every $20.83\mu s$, which corresponds (remembering that the velocity of the receiver: v=1.39m/s) to a distance of $28.94\mu m$. However, as discussed in section 3.1, it is sufficient to use one snapshot every 5mm. The time needed for the RX to move along this distance is $\triangle t = 3.6ms$ or, expressed in samples

$$\triangle n_s = \triangle t \cdot f_s = 172.8 \approx 173. \tag{60}$$

The question of how this lack of measurements could be handled is important. The first thought could lead to the idea to simply select the same impulse response during $\triangle n_s - 1$ time instances and then switch to next next one (c.f. zero-order hold). Although this approach is simple and easy to implement, it has a major drawback: The switching from one impulse response to another presents a discontinuity which causes sidelobes in the spectrum. In fact, keeping the impulse responses constant over the mentioned time span is equivalent to rectangular windowing in time domain, so in frequency-domain the caracteristical sinc-spectrum will be visible. The solution is found by linearly interpolate between two consecutive snapshots in time domain (c.f. first-order hold). Although this solution increases the needed computational complexity drastically, it is necessary in order to obtain a appropriate channel model that behaves similarly to its real existing, physical equivalent.

3.7.2 Memory requirements

As mentioned in Section 3.7.1, the necessity of interpolating between the consecutive measured channel impulse resonses increases the needed memory requirements drastically. For both scenarios, LOS and NLOS, the trajectory that the RX moves along has a length of $\triangle s$=2m. With a chosen step size of $\triangle x_s = 5mm$ between two consecutive measurements, the number of snapshots is $N_{ss} = \frac{\triangle s}{\triangle x_s} = 400$. Equation (60) shows that the time past from one snapshot to the next one (denotes as $\triangle n_s$) is about 173 samples. Therefore, it is necessary to interpolate 172 samples in between. The size of the resulting channel impulse response matrix is then $N_{mat} \times M_{mat}$, with $N_{mat} = N_{ss} \cdot \triangle t_s = 69200$ and $M_{mat} = f_s \cdot \tau_{max} = 12000$ with $\tau_{max} = 0.3s$ as the maximum excess delay in the NLOS scenario (Figure 17). As MATLAB saves the numerical values of the matrix as datatype *double* which allocates S_{double} = 8bytes of memory, it requires

$$S_{mem} = N_{mat} \cdot M_{mat} \cdot S_{double} = 6.64 GByte \tag{61}$$

of memory to allocate the memory needed for the matrix. This memory requirements were also observed during the channel simulations.

4 System design

In this chapter, the design of an adequate transmission system for the acoustic channel is discussed. The transmission system has been designed for a receiver velocity of 1.39m/s (= 5km/h), the same value for which the Doppler spectra and the resulting channel coherence times were obtained (cf. subsection 3.3.3). One of the main goals when designing a transmission system, apart from the aim to achieve a high data rate, is to establish a reliable transmission even in the presence of interference as well as noise, etc. In other words: the system shall provide a low bit error rate (BER). In order to meet this requirement, the question of which modulation scheme can be implemented is crucial.
In Table 4, the values for channel coherence bandwidth B_c, channel coherence time T_c as well as the ones for the RMS Delay Spread τ_{rms} and RMS Doppler Spread ν_{rms} for a frequency of 20kHz, obtained in Chapter 3, are summarized.

Scenario	T_c [ms]	τ_{rms}[ms]	B_c [Hz]	ν_{rms}[Hz]
LOS	19.4	33.9	5.9	51.7
NLOS	23.1	39.4	5.1	43.3

Table 4: Obtained values for the channel coherence bandwidth and channel coherence time

These values present a big impairment for the object of designing a transmission scheme. For higher-order modulation schemes, such as (N-)QAM or PSK, in order to be able to implement a "simple" optimal coherent receiver, it would be necessary to implement a scheme with pulses which fulfill the conditions

$$B_p < B_c \tag{62}$$

and

$$Ts < T_c, \tag{63}$$

where B_p represents the pulse bandwidth and T_s the signal time duration [5]. However, due to the Doppler effect, the received pulses are shifted and spread in frequency domain, reaching values which exceed by far the limit of the condition in (62) when looking at the values of ν_{rms} in Table 4. Considering the RMS Delay Spread τ_{rms}, it becomes also evident that the condition in (63) cannot be fulfilled. Schemes where the signal amplitude levels carry the information are not feasible because of the violation of the second condition. When the signal duration is longer than the RMS Delay Spread, a fading dip will most probably occur during the symbol period, corrupting the received signal's amplitude severely and leading to a wrong decision, which bit was sent at the TX. Recalling that the channel coherence bandwidth is a statistical measure for the range of frequencies over which the channel passes all spectral components with approximately equal gain and linear phase, it becomes evident that also phase modulation schemes are not appropriate for this channel. Based on this

knowledge, the implementation of a robust, *non-coherent* modulation scheme where no phase information of the carrier frequency is sent, becomes inevitable. Taking in account the high values of the delay spread, it becomes evident that impulse radio implementations could only provide a very low data rate as they occupy the whole available bandwidth sending just one symbol at a time. With a maximum excess delay reaching up to 300ms, this would lead to a data rate of about 3bit/s. A transmission scheme should therefore make use of many bandlimited carriers, exploiting the advantage of a very large bandwidth. Hence, the decision was made to implement a *Multicarrier Binary Pulse Position Modulation (Multicarrier BPPM)* scheme. In this scheme, a symbol period is divided in two time slots. Depending on the value of the databit, a pulse, modulated with a certain carrier frequency, is positioned either in the first or in the second time slot. Therefore, the receiver collects the energy at this carrier located in both time slots and decides by simple energy comparison if the sent bit is a 'zero' or a 'one'. This scheme will be explained in more detail in subsection 4.2. The advantage of BPPM in comparison to *On-Off-Keying (OOK)* is that the decision is reduced to a greater/lower-comparison, whereas for OOK the process of finding an adequate decision-threshold would be complicated and most likely lead to a higher BER, considering the given channel.

Comparison with the RF channel

In section 2 it was shown that the audio channel over which the transmission system was implemented can be compared to an RF UWB channel with a frequency range from 17.49MHz to 17.49GHz (see Table 1). It seems natural at this point to ask how the channel parameters of the given channel for electromagnetic wave propagation would look like. Asuming a receiver speed of 1.39m/s (= 5km/h) and dividing the value of τ_{rms} for the audio case by the correction factor k (3), the channel parameters shown in Table 5 are obtained. The RMS Doppler spread has the same value as in the audio channel, therefore also the channel coherence time is the same. Due to the much higher propagation speed of the electromagnetic waves, the RMS delay spread is much smaller, with values in the order of nanoseconds. Therefore, the resulting channel coherence bandwidth B_c is 5.2 MHz for the LOS case and 4.4MHz for NLOS. With these values the conditions in (62) and (63) could easily be fulfilled. Hence, for the RF channel the implementation of higher-order modulation schemes and coherent detectors would be possible.

Scenario	T_c [ms]	τ_{rms}[ns]	B_c [MHz]	ν_{rms}[Hz]
LOS	19.4	38.8	5.2	51.7
NLOS	23.1	45.1	4.4	43.3

Table 5: Equivalent channel parameters for the RF UWB channel for a receiver speed of 1.39m/s

The values from Table 5 show that, in the RF channel, a receiver speed of 1.39m/s would not cause the same problems as in the audio channel due to the much higher wave propagation speed. To obtain the values of the RF channel which correspond to the measured audio channel, also the movement speed has to be corrected by multiplying it with k. Thus, the equivalent movement speed is $v_{RF} = k \cdot v = 1.22 \cdot 10^6$m/s ($= 4.37 \cdot 10^6$km/h). The corresponding channel parameters are shown in Table 6. The equivalence becomes evident when the ratio between B_c and ν_{rms} as well as between T_c and τ_{rms} is considered and compared to the ones from the audio channel (Table 4).

Scenario	T_c [ns]	τ_{rms}[ns]	B_c [MHz]	ν_{rms}[MHz]
LOS	22.1	38.8	5.2	45.2
NLOS	26.4	45.1	4.4	37.9

Table 6: Equivalent channel parameters for the RF UWB channel for a receiver speed of $1.22 \cdot 10^6$m/s

4.1 Signaling

For the chosen multicarrier BPPM, one symbol duration of the sent signal can be expressed as

$$x(t) = Re\left\{\sum_{k=1}^{Nc} g(t - s_k \cdot \tau_s) \cdot e^{j2\pi f_k \cdot t}\right\} \tag{64}$$

where N_c denotes the number of carriers, $g(t)$ the pulse shape of the baseband waveform, s_k the binary value of the k-th bit, τ_s the length of one time slot (=1/2 symbol period) and f_k the carrier frequency of the k-th carrier. If the bit s_k has the value 0, then the first time slot is used, if s_k is 1, the pulse is shifted by τ_s and is therefore set in the second time slot. Then it is multiplied (shifted) to the carrier frequency f_k. For the more general case of N symbol durations, (64) becomes

$$x(t) \quad = \quad Re\left\{\sum_{i=0}^{N}\sum_{k=1}^{Nc} g(t - (2i + s_{k+i \cdot Nc}) \cdot \tau_s) \cdot e^{j2\pi f_k \cdot t}\right\}. \tag{65}$$

Due to the fact that in this modulation scheme pulses are transmitted at the same time in different frequency bands, it is necessary to create bandlimited pulses which do not interfere with each other or at least minimize this effect, the so called *inter-carrier interference (ICI)*. In this section the pulse shapes used in the transmission system are presented.
The pulse shape is a question which considers evaluation. In this work, three different pulse shapes were studied: the raised-cosine pulse, a rectangular pulse filtered by a raised-cosine filter and a Gaussian pulse. First, the raised-cosine filter is shortly explained. The raised-cosine filter is a frequently used filter

which belongs to the Nyquist class (zero ISI at sampling instances). Its transfer function is defined as

$$H(f) = \begin{cases} 1 & \mid f \mid < 2W_0 - W \\ \cos^2\left(\frac{\pi}{4}\frac{\mid f \mid + W - 2W_0}{W - W_0}\right) & 2W_0 - W < \mid f \mid < W \\ 0 & \mid f \mid > W, \end{cases} \tag{66}$$

where W is the absolute bandwidth and W_0 is the minimum Nyquist bandwidth [5]. The corresponding impulse response $h(t)$ is

$$h(t) = 2W_0[\mathrm{sinc}(2W_0 t)]\frac{\cos[2\pi(W - W_0)t]}{1 - [4(W - W_0)t]^2}. \tag{67}$$

The so called *roll-off factor* r is defined as

$$r = \frac{W - W_0}{W_0}. \tag{68}$$

Using this filter would lead to a strictly bandlimited signal with the desired bandwidth W, however, the filter impulse response has to be windowed as it has infinite duration and is therefore not realizable. Limiting the duration of the impulse response is equivalent to a multiplication with a rectangular pulse in time domain, therefore the resulting transfer function is not strictly bandlimited as it shows the characteristical sinc-sidelobes. Figure 30 shows the impulse response of the causal raised-cosine filter with a single-sided bandwidth of W_0=50Hz and r=0.2 (therefore, W=60Hz). The duration of the impulse response was limited to $6T_i$ (T_i=$1/(2 \cdot W_0)$), so for the given filter the time duration is 60ms.

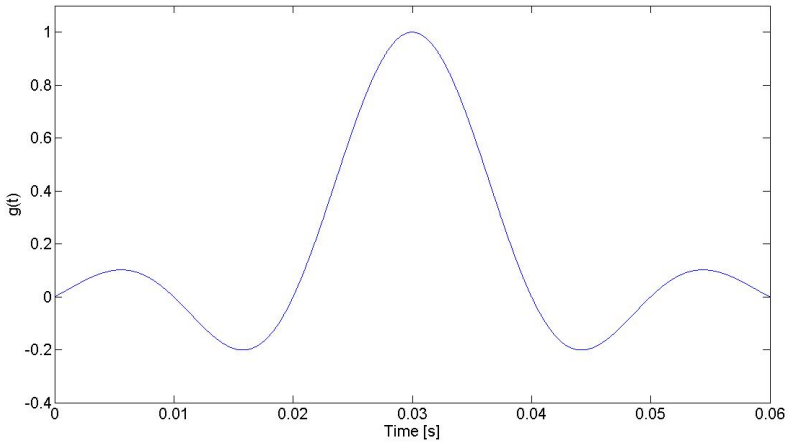

Figure 30: Raised-cosine pulse in time domain (W_0=50Hz, r=0.2)

Figure 31 shows the corresponding spectrum of this pulse. The upper half of the image shows the spectrum in linear scale where the shape of the spectrum and the bandlimitation of ±60Hz can be seen. The desired bandwidth of 120Hz is indicated by two vertical dot-dash lines. The lower part of the image again shows the spectrum of the pulse, but in logarithmic scale. The mentioned sinc-sidelobes, caused by the windowing of the impulse response in time domain, are clearly visible.

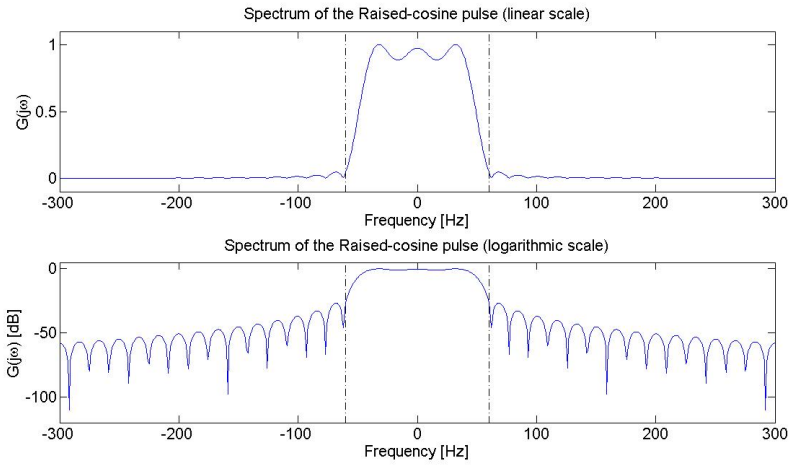

Figure 31: Spectrum of the Raised-cosine pulse (W_0=50Hz, r=0.2)

In Figure 32, a rectangular pulse with 10ms duration filtered by the specified filter in (66) is shown in time domain. Due to the properties of the convolution, the duration of the resulting signal is the sum of the durations of the rectangular signal and the impulse response of the filter minus one sample, so neglecting the duration of this one sample, the filtered signal has a length of 70ms. Figure 33 illustrates the corresponding spectrum, where the sidelobe supression of the rectangular pulse (the well known sinc-spectrum) becomes visible.

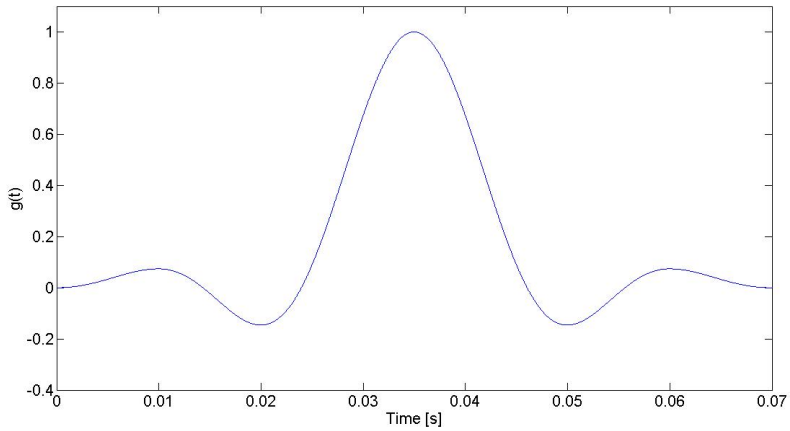

Figure 32: Raised-cosine filtered rectangular pulse in time domain

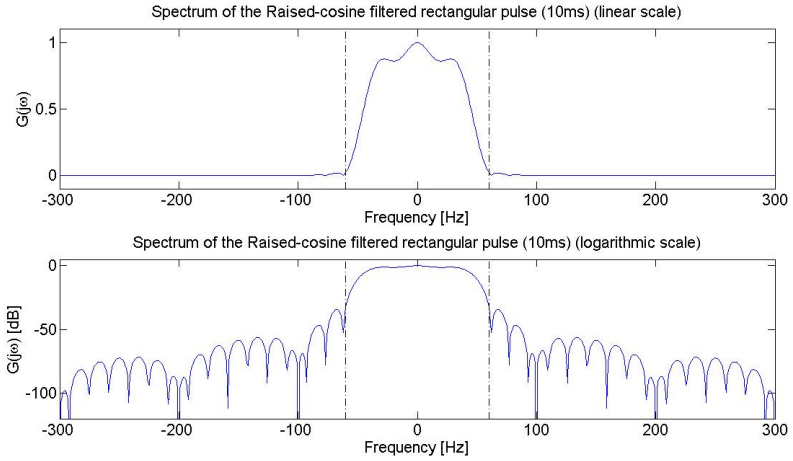

Figure 33: Spectrum of Raised-cosine filtered rectangular pulse

For simplicity reasons, from this point on, the pulse in Figure 32 will be referred to as *RC filtered rectangular* pulse, the one in Figure 30 will be denoted as *Raised-cosine pulse*. The Raised-cosine pulse is shorter in time-domain, causing less ISI, the RC filtered rectangular pulse has lower sidelobes and causes therefore less ICI. The third implemented pulse shape is a Gausspulse with duration of 60ms (same as for the Raised-cosine pulse). It is generated by filtering a Dirac-impulse with a Gaussian Filter whose impulse response can be written as

$$h(t) = e^{-\frac{1}{2}(\alpha \frac{t}{Ti/2})^2} \tag{69}$$

with α=2 and Ti=30ms. This Gausspulse and its spectrum are shown in Figure 34 and 35. The Gausspulse shape yields also a Gaussian pulse-shaped spectrum. To be able to compare the performance of this pulse with the other two ones, its duration was also limited to 60ms, causing sidelobes in the spectrum, but in comparison with the other pulseshapes, the value of these sidelobes is clearly below the ones seen before.

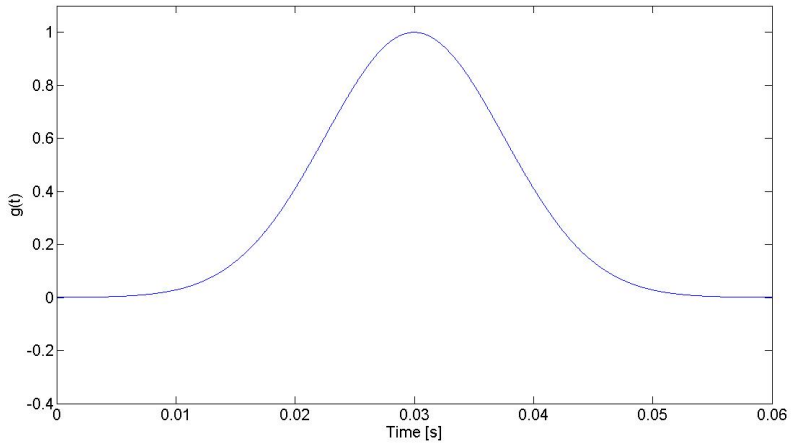

Figure 34: Gausspulse in time domain

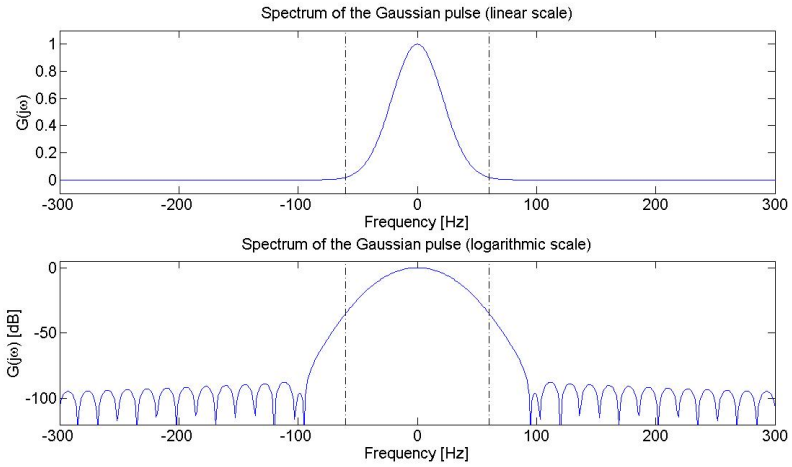

Figure 35: Spectrum of the Gausspulse

4.2 Transmitter

As already mentioned, the modulation scheme for the implementation of the transmission system was chosen to be Multicarrier BPPM. In a BPPM scheme, every symbol period is divided into two time slots of equal size. Depending on which bit was sent, the pulse is set either in the first or the second time slot. The receiver captures the energy of each time slot and performs a comparison whether there is more energy detected in the first or in the second time slot. In order to exploit the large given bandwidth, in the Multicarrier BPPM, this scheme is implemented on many carriers, all sending at the same time in different frequency bands.

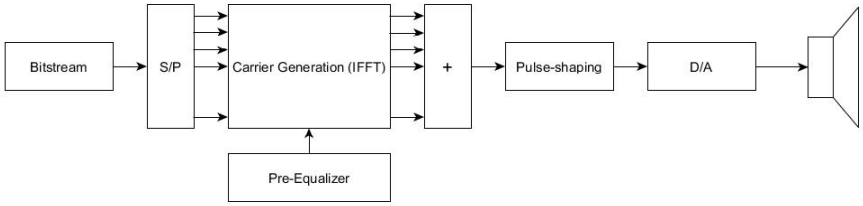

Figure 36: Block Diagram of the transmitter

Figure 36 shows the block diagram of the transmitter. In the following, a short description of every block is given. The *bitstream* represents the data source which provides the data to be transmitted over the channel. In order to transmit the bits from the bitstream over N_c carriers, they are serial-to-parallel converted to N_c parallel bitstreams in the S/P-block, each one with a bit rate R_b/N_c. In the block *Carrier Generation (IFFT)*, N_c parallel sine-carriers are generated and situated in the corresponding time slot, depending on the value of the input bit. The generation is performed using the Inverse Fast Fourier Transform (IFFT). Setting the frequency bin of the desired frequency to 1 and all other bins to 0 and transforming the signal to time domain gives as a result a complex carrier wave. The real value of this carrier is then used for further processing. As the channel exhibits a strong lowpass characteristic, shown in Section 3.4, it is necessary to implement a *Pre-Equalizer*. In this block, every carrier is multiplied with the reciprocal of the measured value of the channel transfer function at this frequency. The average energy should remain unchanged, so therefore the resulting carriers are multiplied with an adequate energy correction factor. The so generated parallel carriers are summed up and processed in the *Pulse-shaping* block, applying the pulse shaping explained in Section 4.1. Then the digital signal is transformed into an analog waveform in the D/A block, which represents the sound card. Finally, transforming the

Group	Frequency band (Hz)	ν_{max} (Hz)	$\triangle f_c$ [Hz]
1	100<f≤1k	4.05	140
2	1k<f≤4k	16.2	160
3	4k<f≤6k	24.3	180
4	6k<f≤9k	36.5	200
5	9k<f≤11k	44.6	220
6	11k<f≤13.5k	54.7	240
7	13.5k<f≤16k	64.8	260
8	16k<f≤18.5k	75	280
9	18.5k<f≤20k	81	300

Table 7: Carrier groups and their frequency spacing

obtained signal to acoustic waves and sending them over the channel is done by a speaker, the last block in Figure 36. The block diagram does not include a block for synchronization, as the synchronization only takes place at the beginning of the transmission. The synchronization consists of a preamble of sent rectangular pulses, indicating the beginning of the data transmission which the receiver can detect to set its timing appropriately.

4.2.1 Frequency spacing of the carriers

In this subsection the frequency spacing necessary to avoid (or at least minimize) inter-carrier-interference will be discussed. As the signal undergoes frequency-shifts and -spread due to the Doppler effect when transmitted over the channel, it is necessary to separate the carriers in frequency domain sufficiently to avoid that the signals of different carriers interfere with each other when they are being spread. Recalling that the Doppler effect depends on the carrier frequency, this leads to a nonuniform frequency spacing. Low-frequency carriers suffer a relatively small Doppler shift, which provides the possibility to apply a narrow frequency spacing. For high-frequency carriers the spacing has to be bigger. The frequency band from 100Hz to 20kHz was divided into 9 groups, assigning a certain frequency spacing to each group, depending on their maximum Doppler shift. The frequency-spacing between two adjacent carriers is

$$\triangle f_c = (2W + 2\nu_{max} + B_G) \mathrm{mod}(f_{res}), \tag{70}$$

where B_G is the additional guard band and f_{res} the desired minimum stepwidth for the frequency spacing. f_{res} was set to 20Hz, so the spacing between two carriers is always a multiple of 20Hz. The corresponding values for B_G were set to fulfill the condition in (70), in general values of about 10Hz. Table 7 shows the carrier groups, their frequency bands, the highest occurring Doppler shift in this band and the frequency spacing within the group. With these values for the frequency spacing, it is possible to assigne N_c= 95 carriers in the whole frequency band for the transmission system. To visualize the sent signal and its frequency spacing, Figure 37 shows a so called *spectrogram*. A spectrogram is a

time-varying spectral representation showing the spectral density of a signal as a function of time, indicating the spectral density by colors. The horizontal axis of the image represents the frequency range, from 0 to 24kHz, the vertical axis denotes the time. Along the frequency axis the increasing carrier separation is easily visible, at low frequencies the spacing is small, where for frequencies near 20kHz the distances between two adjacent carriers are big. Also, the transmission scheme with its time slots, where the pulses are placed depending on the sent bit, becomes immediately clearer. Observing and comparing the values of the spectral density between carriers at low frequencies and the ones located at high frequencies, also the non-uniform power distribution due to the pre-equalizer becomes visible.

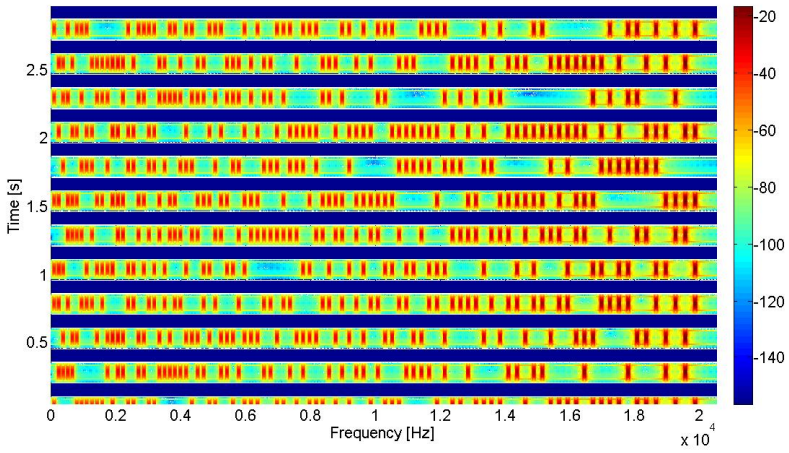

Figure 37: Spectrogram of a sent signal

Figure 38 shows the spectrum of the pre-amplified carriers. As mentioned in Section 4.2, each carrier is multiplied with an energy factor in order to compensate for the lowpass behavior of the channel. The energy factor is therefore the reciprocal of the value of the average CTF at the specified carrier frequency divided by the average carrier energy. Therefore, the average sent energy is the same as before the pre-equalization. The average amplitude level is indicated in the picture by the dashed line.

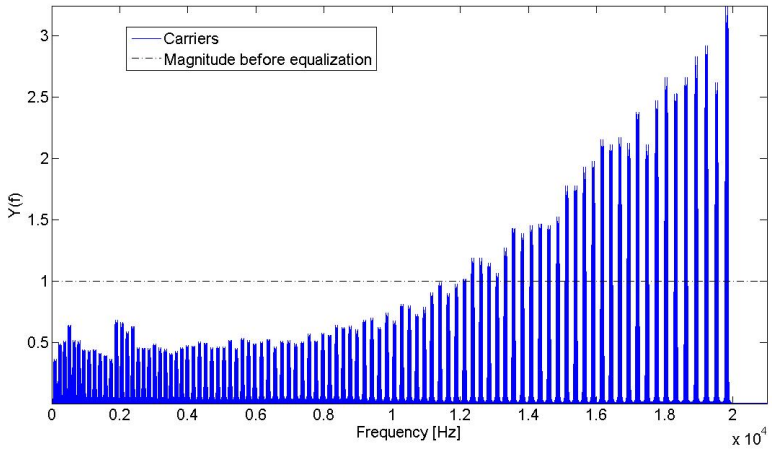

Figure 38: Spectrum of a sent signal

4.2.2 Symbol rate per carrier

One of the properties of the given channel is its reverberant nature, leading to long excess delays due to the relatively small propagation speed of the reflected waves. Therefore, the symbol rate per carrier is very limited because otherwise consecutive pulses would overlap (*intersymbol interference, ISI*) and cause performance degradation w.r.t. the BER. Recalling the Figures 16 and 17, the maximum excess delay for the LOS case is about 230ms, in the NLOS scenario approximately 300ms. When asking for ISI-free transmission and taking into account that the received signal's length is the sum of the maximum excess delay (= the length of the IR) and the pulse duration (60 and 70ms), the maximum symbol rate per carrier r_c has to be set to 1 symbol/s (remembering that one symbol consists of two time slots). Therefore, for a number of 95 carriers (subsection 4.2.1), the achievable data rate would be limited to just 95 bits/s. However, when easing the restriction and allowing ISI, also higher symbol rates can be obtained. After 100ms, the LOS APDP in the Figure 16 shows a power level about 33dB below the maximum value (about 18dB in the NLOS case, Figure 17), after 150ms, the power level has fallen to approximately -40dB (-24dB for NLOS). Therefore, at least for a data rate of 2 symbols/s, the performance degradation due to ISI can be assumed to be low. In Chapter 5, the simulation results for symbol rates of 1, 2, 3 and 4 symbols/s are shown.

4.3 Receiver

In this section, the description of the receiver structure is provided. The receiver was implemented as a frequency separating energy detector. Therefore, for every symbol, the energy on each carrier is collected during the first and the second time slot. The decision, which bit was sent, is made by comparing the captured

energy. Mathematically expressed, the energy in the first time slot can be written as

$$\underline{z}_1 = \sum_{k=1}^{N_c} \left(\sum_{n=n_1}^{n_1+N_I} \left(\left(y[n] \cdot e^{j2\pi f_k \cdot n} \right) \star \Pi_k[n] \right)^2 \right) \cdot \underline{e}_k \tag{71}$$

where $\underline{z}_1$ is a vector containing the energy of every one of the N_c carriers. Furthermore, $\star$ denotes the convolution operator, n_1 the first sample of the first time slot, N_I the length of the integration window expressed in samples, $\Pi_k[n]$ represents a zero-phase rectangular window in frequency domain and $\underline{e}_k$ the k-th unit vector. The width of $\Pi_k[n]$ is given as $2W + 2\nu_{max,k}$, where W denotes the single-sided bandwidth of the received pulse shape and $\nu_{max,k}$ is the maximum Doppler spread of the frequency group to which the k-th carrier belongs (see Table 7). By shifting the received signal $y[n]$ down by the value of its carrier frequency and applying the filtering (the convolution in time domain corresponds to a multiplication in frequency domain), only the pulse on the k-th carrier is obtained. Squaring it gives the signal energy which is summed up over the integration intervall. In fact, the receiver only computes the FFT over the given block length and then uses only the frequency bins of the frequency range of interest. The energy over the second time slot can analogous be written as

$$\underline{z}_2 = \sum_{k=1}^{N_c} \left(\sum_{n=n_2}^{n_2+N_I} \left(\left(y[n] \cdot e^{j2\pi f_k \cdot n} \right) \star \Pi_k[n] \right)^2 \right) \cdot \underline{e}_k \tag{72}$$

where n_2 is the first sample of the second time slot. The decision variable vector $\underline{z}$ is then computed by

$$\underline{z} = \underline{z}_1 - \underline{z}_2, \tag{73}$$

and the detected symbol vector $\underline{u}$ containing all the N_c detected symbols with the elements

$$[\underline{u}]_k = \begin{cases} 0, & [\underline{z}]_k > 0 \\ 1 & \text{else} \end{cases} \tag{74}$$

The system architecture of the receiver is shown in Figure 39.

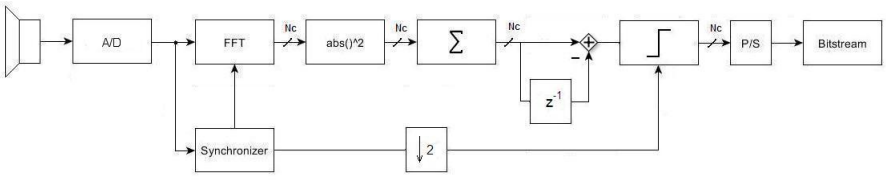

Figure 39: Block Diagram of the receiver

In the first block, the acoustic signal is transformed back into an electrical waveform using a microphone. The waveform is amplified and sampled in the

following A/D block. For simplicity, input filters and amplifiers are also modeled into this block. The sampled pulse train is then processed in the FFT-block, performing a Fast Fourier Transform (FFT) on each block of given size. The magnitude of the result of the FFT is then squared, giving information about the energy distribution over frequency, in other words, the energy of each carrier in this block. Therefore, the output consists of N_c parallel signals, each one representing the energy of the corresponding carrier. For the duration of a specified integration window, the energy of consecutive blocks is summed up, giving just two output values for each carrier to the *decision*-block: The collected energy in the first and second time slot. By comparing whether the first or the second time slot contains more energy, the detector decides if a 'zero-' or a 'one-'bit was received. Finally, the N_c parallel bistreams, containing the bits according to the decision, are combined by a parallel-to-serial converter (P/S in the block diagram), with the received bitstream as output. The *Synchronizer* recognizes the transmitted synchronization pulses and provides the obtained timing to other processing blocks.

4.3.1 Block size and frequency resolution

The choice of the block size, over which the FFT is calculated, is of special importance for the implementation of the RX. Time and frequency resolution are reciprocally proportional, which presents a certain trade-off. A short window allows to track changes of time-variant signals better, in other words, leads to a high resolution in time domain. On the other hand, it reduces the frequency resolution. With a long window, better frequency resolution is obtained at the cost of lower resolution in time domain. Computing the FFT over f_s samples (where f_s is the sample frequency) gives a frequency resolution of 1Hz due to the properties of the FFT. Reducing the number of points by some certain factor, in other words, reducing the block size, leads to a reduction of frequency resolution by the same factor. For the chosen transmission scheme, the required time resolution is determined by the symbol rate. The block size N_{bl}, expressed in samples, was chosen to be

$$N_{bl} = \frac{f_s}{20} = 2400 \tag{75}$$

where f_s=48kHz is the used sample rate of the transmission system and N_{bl} denotes the block length in samples. Expressed in milliseconds, the block length T_{bl} is

$$T_{bl} = \frac{N_{bl}}{fs} = 50ms \tag{76}$$

and as a consequence, the obtained frequency resolution is

$$f_{res} = \frac{1}{T_{bl}} = 20Hz. \tag{77}$$

It has to be noted that this value was already used in (70), when the frequency spacing between the carriers was assigned.

Scenario	τ_{rms} [ms]	T_I [ms]
LOS	33.9	150
NLOS	39.4	150

Table 8: Integration window length for LOS and NLOS

4.3.2 Integration window

This subsection discusses the adequate choice of the length of the so called integration window over which the energy of the received signal is summed up. Without the presence of noise, the choice of the length of the integration window, the time duration over which the RX captures the energy on each carrier to detect the value of the sent bits, would be simple. The integration window would be set to the length of one time slot in order to collect all the energy in this slot. In the presence of noise, however, this is suboptimal [12]. The most power of the received pulse, recalling the APDPs, (16) and (17), is concentrated at the beginning of each time slot, while at the end only strongly attenuated MPC arrive the RX. Therefore, the noise power captured at the end of the time slot may be higher than the signal energy and may furthermore lead to a wrong decision at the detector. According to [12], as a rule of thumb, for a NLOS channel with exponentionally decaying power delay profile

$$h(t) = 1 - e^{T_I/\tau_{rms}} \tag{78}$$

where T_I is the integration interval, it is appropriate to set the integration intervall to about one and a half to two times the RMS Delay Spread τ_{rms}. With this choice, about 80-85% of the received energy is captured, but at most 1-2dB of excess noise. With a pulse duration of 60-70ms and the chosen block length of 50ms of the FFT, which is the minimum resolution in time domain and the values for τ_{rms} from Table 2, the duration of the integration window was set to the values shown in Table 8. It has to be noted that for both scenarios, the integration interval was set to a value slightly higher than 2 times the RMS Delay Spread (plus the pulse duration). The reason is that the synchronization of the transmission system does not track the slightly shifted arrival time of the incident waves when the RX moves away from the TX and, as a consequence, the integration window is set too early (about 6ms for the most distant point). In order to compensate for that, the integration interval was set longer than the recommended duration.

5 Receiver performance evaluation

In this chapter, the performance of the digital transmission system presented in Chapter 4 will be evaluated by sending data with different pulse shapes, transmission speeds and carrier spacings over the simulated channel (Section 3.7) and comparing their bit error rate. The BER is an important figure of merit in a communication system as it shows the ability of the system to provide a certain reliability of data the presence of additive interference, modeled as Gaussian noise. For the given channel, the BER of the implemented transmission system can be expected to be considerably worse than in a pure additive white Gaussian noise scenario due to the strong signal distortions induced by the channel and due to the non-coherent receiver. These distortions are shown in Figure 40. The lower half of the image shows the spectrogram of a received signal (with 2Symb/s per carrier) after being sent over the simulated NLOS channel. When comparing it with the sent signal, shown in the upper part of the image, severe signal distortion becomes evident. On one hand, the delay spread and therefore slightly overlapping pulses are visible, on the other hand the frequency spreading of the pulses due to the Doppler effect can be observed.

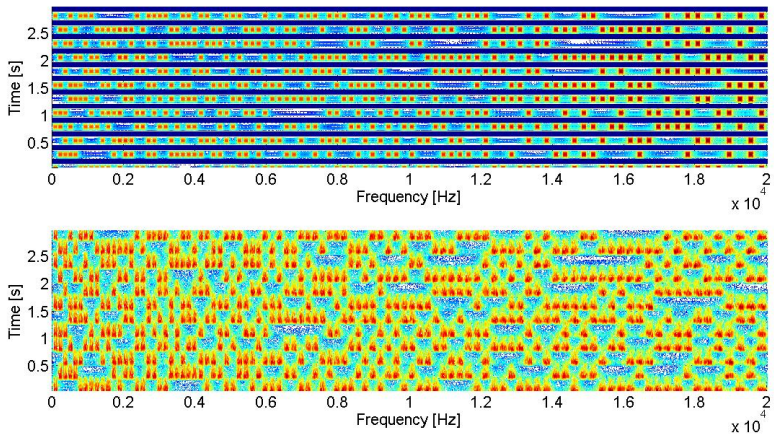

Figure 40: Spectrogram: Comparison of sent and received signal

BER

In Section 4.1, pulse shapes and corresponding spectra of different pulses were shown. Figure 41 illustrates the bit error curves for these different pulse shapes with a transmission speed of r_c =2 symbols/s on each carrier for both the LOS and the NLOS scenario. The LOS-curves are indicated by a '+'-sign at the measured points, whereas the NLOS-curves are displayed with a "diamond"-sign. Regardless of the pulse shape, the bit error rate is slightly lower in the LOS scenario where the signal spreading in frequency domain is lower and, due to the

slightly lower delay spread, ISI is reduced. In both scenarios, the Raised-cosine pulse shows the lowest bit error rate, followed by the RC-filtered rectangular pulse. The Gaussian pulse, although having the lowest sidelobes and therefore causing the lowest ICI, exhibits the highest bit error rate of the implemented pulse shapes. The illustration also shows the theoretical BER curve of a PPM scheme for an AWGN channel [13]. The difference to the obtained values in the audio channel is huge. Apart from the influence of the non-coherent receiver, there are two main reasons for the relatively bad behavior: The Dopper spread and the time-dispersiveness of the channel. Once again, the Doppler spread presents a big impairment for the transmission system because it spreads the signal's energy in frequency domain. Without the presence of this frequency-shifting and -spreading, it would be sufficient to collect the signal energy of one carrier just over the bandwith of the pulse, mathematically expressed as $B_{rec} = 2W$. B_{rec} denotes the bandwidth over which the receiver sums up the received energy of a carrier and W the one sided bandwidth of the pulse. However, as a consequence of the frequency-shifting and -spreading of the Doppler effect, it is necessary to collect the energy over the pulse bandwidth plus two times the maximum Doppler shift for the given carrier frequency, so $B_{rec,D} = 2W + 2\nu_{max}$. In the presence of noise, this leads to a performance degradation as the receiver sums up more noise energy due to the increased bandwidth. The second reason for the performance degradation, the time-dispersiveness of the channel, forces us to sum up the pulse energy over a longer time span than the pulse duration. As explained in subsection 4.3.2, the length of the integration window was chosen so that it sums up about 80-85% of the signal energy. As a consequence, the rest of the signal energy is lost and due to the longer integration window (which would be just the pulse duration in a AWGN scenario) more noise energy is summed up which again leads to a worse behavior in comparison to a pure AWGN channel.

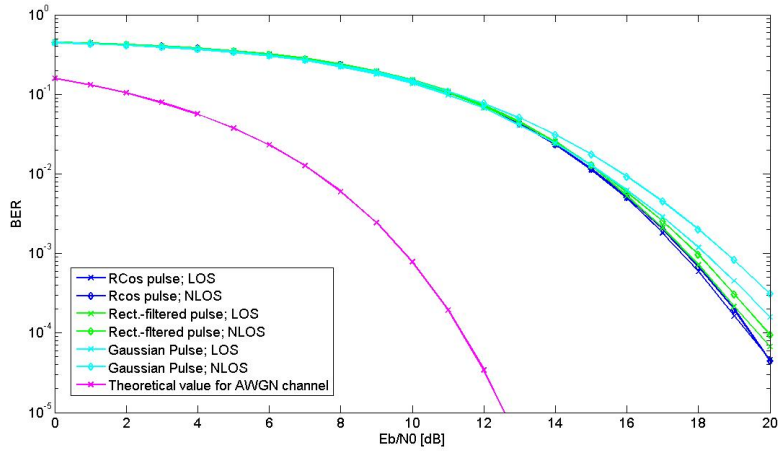

Figure 41: BER for different pulse shapes (2Symb/s per carrier)

As mentioned in subsection 4.2.2, ISI-free transmission would require a symbol rate r_c of just 1 Symbol/s, leading to a data rate of 95bit/s. However, when allowing a certain amount of ISI, it is possible to increase the data rate by implementing higher symbol rates. Figure 42 shows the bit error curves for carrier symbol rates of 1, 2, 3 and 4 symbols/s. In the previous simulation, the Raised-cosine pulse provided the lowest bit error rate, so in this and the following simulation only this pulse is shown.

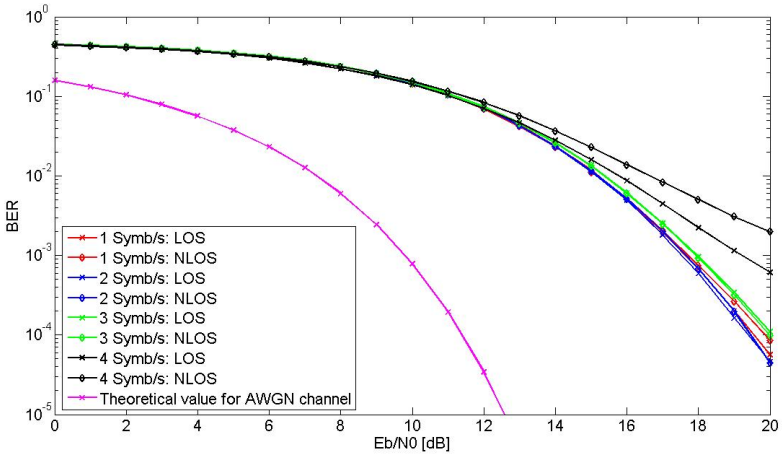

Figure 42: BER for different symbol rates (Raised-cosine pulse)

From the figure it can be seen that up to a symbol rate of 3 symbols/s, the impact of the increased ISI due to the higher symbol rate does not lead to an unacceptable performance loss w.r.t. the BER. In fact, the advantage of being able to transmit data two or three times faster is opposed by only a slightly higher number of bit errors. When considering the possibility of implementing channel coding, with even a high code-rate, in other words, very few redundancy in the sent data stream, the advantages of implementing the scheme with 3 symbols/s predominate clearly. The achievable data rate R_b of the transmission system is therefore $R_b = N_c \cdot r_c = 95 \cdot 3 = 285\text{bit/s}$. If the symbol rate is further increased, the performance degradation becomes severe. When transmitting 4 symbols/s on each carrier, the ISI becomes dominant and an error floor becomes visible. Due to the higher delay spread in the NLOS scenario, the performance degrades faster than in the LOS case. The corresponding data rate for the RF UWB channel can be calculated by multiplying R_b with the correction factor k introduced in section 2. Therefore, the data rate for electromagnetic wave propagation is 249.3Mbit/s for an equivalent receiver speed of $v_{RF} = 1.22 \cdot 10^6\text{m/s}$.

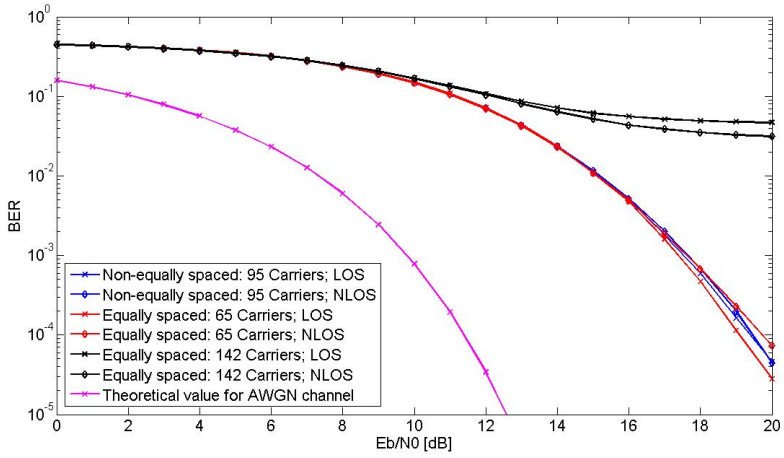

Figure 43: BER for non-equally- vs. equally-spaced carriers (Raised-cosine pulse)

In Section 4.2.1, the decision to implement a non-uniform carrier frequency spacing was made. As explained, the spacing between adjacent carriers was increased with higher carrier frequency values to compensate the increasing effect of the Doppler spread. In order to justifiy this decision and show its validity, two other carrier configurations were introduced. The first one neglects the Doppler effect and uses therefore a constant carrier spacing of $\triangle f_c = 140\text{Hz}$ over the whole usable bandwidth. Therefore, 142 carriers can be placed in the spectrum, leading to a higher achievable data rate. The second one also uses

a constant carrier spacing. This spacing is derived from the highest ocurring Doppler spread and is set to $\triangle f_c = 300$Hz. (Note that this is equal to the biggest carrier spacing in the non-equally-spaced case). Due to the big separation in frequency domain, only 65 carriers can be placed in the spectrum. Figure 43 shows the simulation results for these spacings (with a symbol rate of 2 symbols/s) in comparison with the chosen non-uniform spacing from subsection 4.2.1. As expected, the bit error curves of the non-equally spaced and the equally spaced case with 65 carriers are very similar while the configuration with 142 carriers and low carrier separation exhibits an error floor. Even under "good" conditions with low additive noise, the error rate never drops below $2{\cdot}10^{-2}$. This is the expected result, as the Doppler effect causes strong ICI due to the insufficient carrier separation. It is also remarkable that the error rate is in the NLOS scenario lower than in the LOS case. This can be explained recalling the Doppler Power spectra for both scenarios (Figures 20 and 22). For LOS, the spectra shows one dominant component shifted by the maximum Doppler shift, whereas in the non-line-of-sight scenario the signal is spread more, but less energy is shifted to the maximum value. Therefore, the energy shifted to adjacent frequency bands is less and the resulting BER lower. In summary, the narrow carrier spacing is insufficient and leads to an unacceptable BER. The configuration with high carrier separation gives a similar bit error rate as the one with non-uniform spacing, but at only 2/3 of the data rate.

6 Conclusion

Results

In this thesis the implementation of a non-coherent digital data transmission system over a time-variant indoor audio channel was presented. Because of the lack of adequate channel models to investigate and simulate the behavior of this channel, it had to be sounded, followed by the implementation of a time-variant channel model based on the obtained channel impulse responses. The most important results of this work and possible ways to improve the presented transmission system will be presented in this section.

It was shown that the audio channel has high Doppler spread with an RMS Doppler spread ν_{rms} = 51.7Hz in the LOS scenario and 43.3Hz in the NLOS case. The resulting channel coherence time is therefore 19.4ms and 23.1ms, respectively. The channel also shows a highly time-dispersive behavior, with an RMS Delay spread τ_{rms} = 33.9ms in the LOS case and 39.4ms in the NLOS scenario, leading to a channel coherence bandwidth of 5.9Hz and 5.1Hz, respectively.

Due to the extracted channel parameters, the implementation of a coherent receiver with a higher-order modulation scheme, such as N-QAM, was found to be impossible, therefore a robust, noncoherent Binary Pulse Position Modulation scheme (BPPM) was implemented.

In order to achieve high data rates, the BPPM scheme was implemented on 95 bandlimited carriers (Multicarrier BPPM transmission scheme). The carrier spacing between two adjacent carriers was chosen according to the maximum Doppler shift at the given carrier frequency.

The receiver was implemented as a multichannel energy detector, which sums up the energy of each time slot for every carrier. The decision, which bit was sent, is reduced to a simple threshold-comparison.

Although the given channel, highly time-dispersive, time-variant and with huge Doppler spread, is the worst possible channel to establish a communication system, it is possible to transmit and receive data with a data rate of 285bit/s with a certain data reliability, although the necessary E_b/N_0 has to be notably higher than for other, less challenging channels.

As explained in this work, the audio channel can be compared with the RF UWB channel. The implemented receiver speed of 1.39m/s in the audio channel corresponds to a speed of $1.22 \cdot 10^6$m/s in an RF environment and the obtained data rate of 285bit/s corresponds to a data rate of 249.3Mbit/s.

Further work

It was shown that the channel impulse responses in higher frequency bands decay much faster than in low-frequency bands. This could be used to implement a transmission scheme with different symbol rates on each carrier and thereby increase the achievable data rate.

The used modulation scheme was chosen to be multicarrier BPPM. The data rate could be doubled by implementing on-off-keying (OOK) instead. The difficulty of this possible implementation lies in finding an adequate decision threshold for each carrier.

The implemented time-variant channel model can be used and adapted. For example, with small modifications, the simulation of different, lower movement velocities is easily possible in order to implement a transmission scheme for a lower, more realistic Doppler spread. Therefore, the obtained results would be more comparable to the ones of an actual implementation in the RF channel. When reducing the speed of movement between transmitter and receiver, and therefore reducing the values of the Doppler spread, also the implementation of other modulation schemes is possible. Furthermore, a performance improvement w.r.t. the BER can be expected.

A Appendix

A.1 Illustrations of the physical channel setup and the used software

The Figures 44-46 show the measurement equipment, environment and setup.

Figure 44: Picture of the used speaker, Yamaha MSP5

Figure 45: Picture of the used microphone, Behringer ECM8000

Figure 46: Picture of the measurement setup

In the Figures 47-49, the settings of the used recording software (Audacity) and audio interface (Fireface 800) for the measurement campaign is shown.

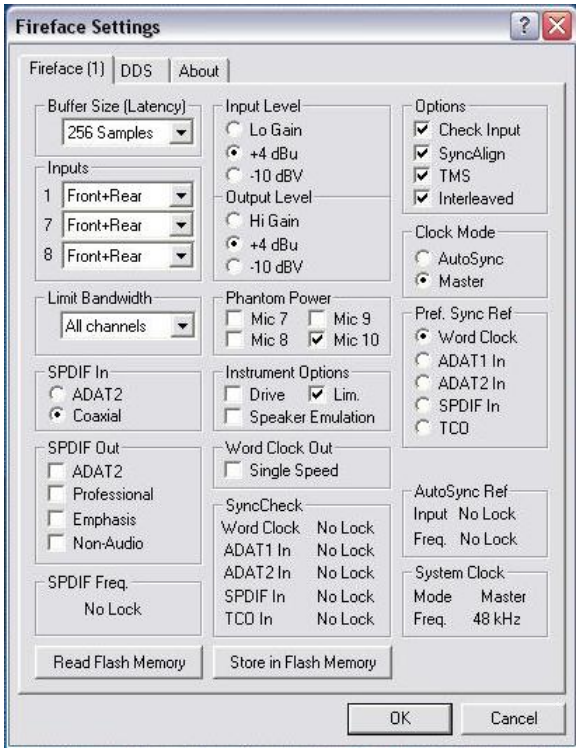

Figure 47: Screenshot of the settings panel of the audio interface, Fireface 800

Figure 48: "Devices"-settings of the recording software, Audacity

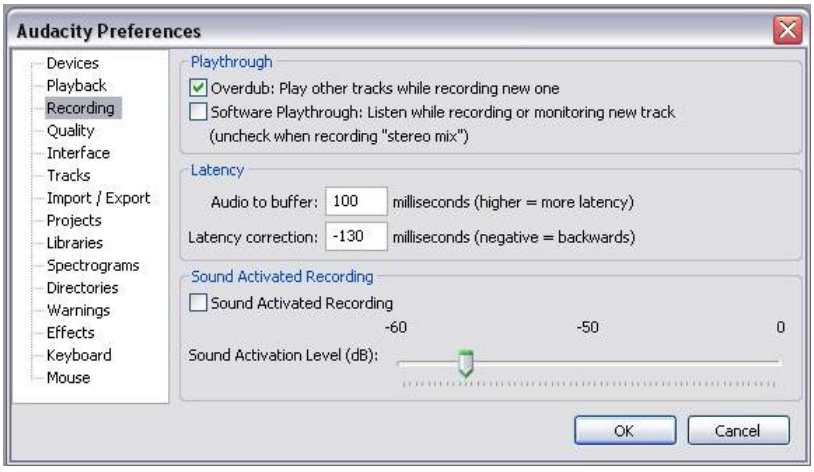

Figure 49: "Recording"-settings of Audacity

A.2 Datasheets

MEASUREMENT MICROPHONE ECM8000

ENGLISH

Technical Specifications

Version 1.2 July 2000

MEASUREMENT MICROPHONE

FEATURES

- ▲ Precise electret condenser measurement microphone
- ▲ Ultra-linear frequency response
- ▲ Well-balanced, true omni-directional pattern
- ▲ Optimally suited for room correction applications
- ▲ Phantom powered, +15 V to +48 V
- ▲ Rugged construction and sleek, modern design
- ▲ Microphone stand adapter and windscreen for outdoor measurement included
- ▲ Perfect for use with the ULTRA-CURVE DSP8000 / ULTRA-CURVE PRO DSP8024 or any other real-time analyzer
- ▲ Manufactured under the BEHRINGER quality control

SPECIFICATIONS

Type	electret condenser, omni-directional
Impedance	600 Ohms
Sensitivity	-60 dB
Frequency response	15 Hz to 20 kHz
Connector	gold-plated XLR
Phantom power	+15 V to +48 V
Weight	app. 120 g

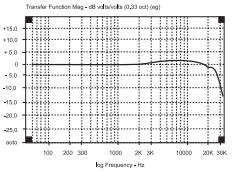

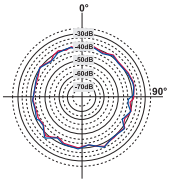

BEHRINGER is constantly striving to maintain the highest professional standards. As a result of these efforts, modifications may be made from time to time to existing products without prior notice. Specifications and appearance may differ from those listed or illustrated.

BEHRINGER Spezielle Studiotechnik GmbH, Hanns-Martin-Schleyer-Str. 36-38, 47877 Willich-Münchheide II, Germany
Tel. +49 (0) 21 54 / 92 06-0, Fax +49 (0) 21 54 / 92 06-30

BEHRINGER

www.behringer.com

Figure 50: Datasheet of the used microphone, Behringer ECM 8000

MSP STUDIO Series

Powered Near-field Monitors

MSP7 STUDIO

MSP7 STUDIO Rear Panel

MSP5 STUDIO

MSP5 STUDIO Rear Panel

SW10 STUDIO

SW10 STUDIO Rear Panel

Refined Monitoring Precision

Powered Monitor Speaker MSP7 STUDIO

- 2-way bass-reflex bi-amplified near field studio monitor 6.5" cone woofer and 1" titanium dome high-frequency unit delivers 45Hz- 40kHz frequency response.
- 130 watts (LF 80W + HF 50W) dynamic bi-amplified power.
- XLR balanced input.
- Advanced Magnetic Structure Design
- One-piece Molded Enclosure with Rounded Baffle
- 31 positions Level Control facilitates precise overall system level matching.
- Low Cut switch and TRIM Control (High/Low).
- Full magnetic shielding.

Powered Subwoofer SW10 STUDIO 10" bass-reflex powered subwoofer delivers solid 25Hz- 150Hz frequency response.

- 180 watts dynamic power.
- XLR balanced inputs (L/R/SUBWOOFER) .
- XLR balanced outputs(L/R/SUBWOOFER) parallel connection with input signals.
- Level control facilitates precise system level controls.
- 40-120 Hz, 80 Hz at Center Click LPF controls.
- Phase switch simplifies phase allignment.
- Full magnetic shielding.

Powered Monitor Speaker MSP5 STUDIO

- 2-way bas-reflex bi-amplified near field studio monitor 5" cone woofer and 1" titanium dome high-frequency unit delivers 50Hz- 40kHz frequency response.
- 67 watts (LF 40W + HF 27W) dynamic bi-amplified power.
- XLR balanced input and 1/4" unbalanced input.
- Advanced Magnetic Structure Design
- One-piece Molded Enclosure with Rounded Baffle
- 31 positions Level Control facilitates precise overall system level matching.
- TRIM Control(High/Low).
- Full magnetic shielding.

OPTIONS (MSP7 STUDIO)

BWS50-190/260
Wall Bracket

OPTIONS (MSP5 STUDIO)

BCS20-150/210
Ceiling Bracket

Figure 51: Datasheet of the used speaker, Yamaha MSP5 (page 1)

MSP STUDIO Series

SPECIFICATIONS

MODEL			MSP7 STUDIO	MSP5 STUDIO	SW10 STUDIO
GENERAL	Type		Bi-amp 2-way Powered Speaker	Bi-amp 2-way Powered speaker	Powered subwoofer
	Crossover Frequency		2.5 kHz LF:30dB/oct, HF:30dB/oct	2.5 kHz LF:24dB/oct, HF:24dB/oct	-
	Overall Frequency Response		45Hz-40kHz (-10dB)	50Hz-40kHz (-10dB)	25Hz-150Hz (-10dB)
	Maximum Output Level		106dB, 1m on Axis	101dB, 1m on Axis	111dB, 1m on Axis
	Dimensions (W x H x D)		218 x 330 x 235mm (8.6" x 13.0" x 9.3")	179 x 279 x 208mm (7.0" x 11.0" x 8.2")	328 x 459 x 476mm (12.9" x 18.1" x 18.7")
	Weight		12.2kg (26.9lbs)	7.9kg (17.4lbs)	26.5kg (58.4lbs)
	Magnetic Shielding		Yes	Yes	Yes (None covered type)
Speaker Section	Components	LF	6.5" cone	5" cone	10" cone
		HF	1.0" Titanium dome	1.0"Titanium dome	-
	Enclosure	Type	Bass-Reflex	Bass-Reflex	Bass-Reflex
		Material	PP	PP	MDF
Amplifier Section	Output Power *	LF	80W THD = 0.05%, RL = 4Ω	40W THD = 0.02%, RL = 4	180W f = 100Hz, THD = 1%, RL = 8
		HF	50W THD = 0.05%, RL = 6Ω	27 W THD = 0.02%, RL = 6Ω	-
	S/N, IHF-A filter		≥99dB, LEVEL = Max	≥94dB, LEVEL = Max	≥100dB, LEVEL = Max
	Input Sensitivity	XLR 3-31	+4dBu, LEVEL = Center -6dBu, LEVEL = Max	+4dBu, LEVEL = Center -6dBu, LEVEL = Max	+4dBu, LEVEL = Center -6dBu, LEVEL = Max
		PHONE	-	10dBu, LEVEL = Cente -20dBu, LEVEL = Max	-
	Input Connectors, Impedance		XLR-3-31 (balanced), 10kΩ	XLR-3-31 (balanced), 10kΩ PHONE (unbalanced), 10kΩ	XLR-3-31 x 3 (balanced), 10kΩ
	Output Connectors		-	-	XLR-3-32 x 3 (balanced), Parallel connection with Input
	Controls	Level Control	31 Positions Detent type VR (Min = -∞Attenuation)	31 Positions Detent type VR (Min = -∞Attenuation)	Center Click VR (Min = -∞Attenuation)
		LOW CUT Switch	FLAT/80Hz (12dB/oct)/100Hz (12dB/oct)	-	-
		HIGH TRIM	+1.5/0/-1.5dB at 15kHz	+1.5/0/-1.5dB at 15kHz	-
		LOW TRIM	+1.5/0/-1.5/-3dB at 45Hz	+1.5/0/-1.5/-3dB at 60Hz	-
		POWER Switch	on/off	on/off	on/off
		PHASE Switch	-	-	Normal/ Reverse
		LPF control	-	-	40-120Hz, 80Hz at Center Click
	Indicators	LED	Green: Power On Red: Clipping	Green: Power On Red: Clipping	Green: Power On Red: Clipping
	Power Consumption		100W	60W	160W

* These specifications apply to rated power supplies of 100, 120, 230 and 240 V.
* Specifications and appearance subject to change without notice.

DIMENSIONS

unit : mm

MSP7 STUDIO

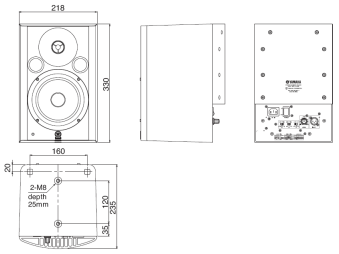

MSP5 STUDIO

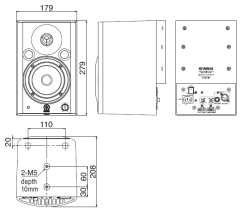

SW10 STUDIO

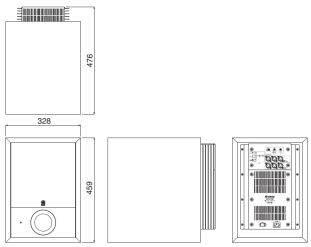

Figure 52: Datasheet of the used speaker, Yamaha MSP5 (page 2)

References

[1] A. F. Molisch, J. R. Foerster, M. Pendergrass, "Channel Models for Ultrawideband Personal Area Networks", *IEEE Wireless Communications*, Vol. 10, No. 6, December 2003

[2] J. Bach Andersen, et al, "Room Electromagnetics", *IEEE Antennas and Propagation Magazine*, Vol. 49, No. 2, April 2007

[3] J. Gruber, *Charakterisierung eines Demonstrationssystems für UWB-Übertragungsstrecken,* Diploma Thesis, Graz University of Technology, 2004

[4] Federal Communications Commission, "Second Report and Order and Second Memorandum Opinion and Order", In: 04-285, Dec. 2004

[5] B. Sklar, *Digital Communications; Fundamentals and Applications*, New Jersey, USA: Prentice-Hall, Second edition, 2001

[6] A. V. Oppenheim, R. W. Schafer, J. R. Buck, *Discrete-Time Signal Processing*, New Jersey, USA: Prentice-Hall, Second edition, 1998.

[7] A. F. Molisch, *Wireless Communications*, John Wiley and Sons, 2006.

[8] D. D. Rife, J. Vanderkooy, "Transfer-Function Measurement with Maximum-Length Sequences", *Journal of the Audio Engineering Society,* Volume 37, Number 6, June 1989

[9] T. S. Rappaport, *Wireless Communications*, New Jersey, USA: Prentice Hall, Second edition, 2002

[10] S. Saleem, C. Vogel, "Active Compensation of Frequency Response in High-Resolution Time-interleaved ADCs using a Low-Resolution ADC and a Time-Varying Filter", *Circuits and Systems (ISCAS),* In *Proc. 2010 IEEE International Symposium on*, pages 561-564, 30 May - 2 June, 2010

[11] Joint Technical Comittee of Committee T1 R1P1.4 and TIA TR46.33/TR45.4.4 on Wireless Access. "Draft Final Report on RF Channel Characterization," Paper No. JTC(AIR)/94.01.17-238R4, January 17, 1994

[12] K. Witrisal, et al, "Noncoherent Ultra-Wideband Systems", *IEEE Signal Processing Magazine*, Vol. 26, Nr. 4, July 2009

[13] M. Hämäläinen, et al., "On the Performance Comparison of Different UWB Data Modulation Schemes in AWGN Channel in the Presence of Jamming", In *IEEE Radio and Wireless Conference, pages 83-86, 2002*